Circumbinary Disk Accretion into Spinning Black Hole Binaries

Federico G. Lopez Armengol[1,2] , Luciano Combi[1,2] , Manuela Campanelli[1] , Scott C. Noble[3] , Julian H. Krolik[4] ,
Dennis B. Bowen[5] , Mark J. Avara[1,6] , Vassilios Mewes[1,7,8] , and Hiroyuki Nakano[9]

[1] Center for Computational Relativity and Gravitation, Rochester Institute of Technology Rochester, NY 14623, USA; fglsma@rit.edu
[2] Instituto Argentino de Radioastronomía (CONICET; CICPBA), C.C. No. 5, 1894 Villa Elisa, Argentina
[3] Gravitational Astrophysics Laboratory, NASA Goddard Space Flight Center Greenbelt, MD 20771, USA
[4] Physics and Astronomy Department, Johns Hopkins University Baltimore, MD 21218, USA
[5] X Computational Physics, Los Alamos National Laboratory Los Alamos, 87545, New Mexico, USA
[6] Institute of Astronomy, University of Cambridge Madingley Road, CB3 0HA Cambridge, UK
[7] National Center for Computational Sciences, Oak Ridge National Laboratory P.O. Box 2008, Oak Ridge, TN 37831-6164, USA
[8] Physics Division, Oak Ridge National Laboratory, P.O. Box 2008, Oak Ridge, TN 37831-6354, USA
[9] Faculty of Law, Ryukoku University Kyoto 612-8577, Japan
Received 2021 January 30; revised 2021 March 5; accepted 2021 March 20; published 2021 May 19

Abstract

Supermassive black hole binaries are likely to accrete interstellar gas through a circumbinary disk. Shortly before merger, the inner portions of this circumbinary disk are subject to general relativistic effects. To study this regime, we approximate the spacetime metric of close orbiting black holes by superimposing two boosted Kerr–Schild terms. After demonstrating the quality of this approximation, we carry out very long-term general relativistic magnetohydrodynamic simulations of the circumbinary disk. We consider black holes with spin dimensionless parameters of magnitude 0.9, in one simulation parallel to the orbital angular momentum of the binary, but in another anti-parallel. These are contrasted with spinless simulations. We find that, for a fixed surface mass density in the inner circumbinary disk, aligned spins of this magnitude approximately reduce the mass accretion rate by 14% and counter-aligned spins increase it by 45%, leaving many other disk properties unchanged.

Unified Astronomy Thesaurus concepts: Accretion (14); Supermassive black holes (1663); Rotating black holes (1406); Magnetohydrodynamical simulations (1966)

1. Introduction

The existence of supermassive binary black holes (SMBBH) is a natural prediction of the current hierarchical models of galaxy formation (Merritt & Milosavljević 2005). After two galaxies merge, there are reasons to think the orbit of the newly formed binary will shrink to a sub-parsec scale by dynamical friction and interaction with surrounding gas (Begelman et al. 1980; Escala et al. 2004, 2005; Merritt 2004, 2006; Dotti et al. 2007, 2009b; Mayer et al. 2007; Shi et al. 2012; Sesana & Khan 2015; Mirza et al. 2017; Khan et al. 2019; Tiede et al. 2020). From then on, the emission of gravitational waves becomes an efficient mechanism for energy and angular momentum extraction until coalescence (Pretorius 2005; Baker et al. 2006; Campanelli et al. 2006). This emission of gravitational waves makes SMBBHs the primary targets in the mHZ frequency window by the future Laser Interferometer Space Antenna (LISA, Amaro-Seoane et al. 2017) and by pulsar timing techniques in the nHz range (Babak et al. 2016; Reardon et al. 2016; Alam et al. 2021).

Unlike stellar-mass binary black hole systems, the environment of SMBBHs might be rich in gas (Barnes & Hernquist 1992, 1996; Mihos & Hernquist 1996; Mayer et al. 2007; Dotti et al. 2012; Mayer 2013; Derdzinski et al. 2019), allowing the system to emit electromagnetic (EM) radiation. Many signatures have been proposed as ways to hunt for SMBBHs in the EM spectrum: periodic light curves in active galactic nuclei (AGNs; Valtonen et al. 2006; Graham et al. 2015a, 2015b; Liu et al. 2019; Saade et al. 2020, interrupted jet activity (Schoenmakers et al. 2000; Liu et al. 2003), traces of jet precession or "spin-flips" in X-shaped radio galaxies (Merritt & Ekers 2002), dual compact radio cores (Rodriguez et al. 2006), shifts in the profiles of broad emission lines

(Bogdanović et al. 2009; Dotti et al. 2009a), X-ray emission from streams striking the accretion disks around the individual black holes or a "notch" in the optical/IR spectrum (Roedig et al. 2014; Krolik et al. 2019). However, it is not at all clear whether any of these can be truly expected. Numerical simulations are key guides to this search because they may unveil unique dynamics and radiative properties.

Matter flows toward these systems through a circumbinary disk because interstellar gas at the center of merged galaxies is expected to have far too much angular momentum to approach the binary directly (Springel et al. 2005; Chapon et al. 2013). Circumbinary disks differ in many respects from accretion disks around single black holes (BHs), especially for mass-ratios close to unity. The most striking differences originate in the strong gravitational torques that the orbiting BHs exert on the surrounding matter. Early one-dimensional work suggested that these torques would prevent any gas from falling toward the binary (Lin & Papaloizou 1979; Pringle 1991), but more recent multi-dimensional simulations showed that most of the externally supplied mass is accreted and an approximate inflow equilibrium can be reached (see, for instance, Artymowicz & Lubow 1996; MacFadyen & Milosavljević 2008; Noble et al. 2012; Shi et al. 2012; D'Orazio et al. 2013; Farris et al. 2014; Shi & Krolik 2015; Zilhão et al. 2015; Miranda et al. 2016; Rafikov 2016; Tang et al. 2017.

These simulations also showed that the circumbinary disk is truncated at a distance $\approx 2b$ from the binary center-of-mass, where b denotes the binary separation. Outside this truncation radius, mass piles up, forming a local peak in the surface density profile; inside this radius, the accretion flow onto the binary is confined within two narrow streams traversing a low-

density gap. Each of these streams is associated with one of the black holes.

These streams are complex systems. A portion of their mass receives enough angular momentum from the binary torques to be flung back to the inner edge, transferring significant amounts of angular momentum to the disk. Their impact can cause a steady growth in an $m = 1$ mode of the azimuthal distribution of matter at the inner edge, giving rise to an orbiting overdensity at $2b < r < 4b$ that can be the dominant source of matter for accretion onto the binary. This is the so-called "lump."

When the accretion streams enter the binary, each feeds a small accretion disk surrounding one of the black holes; the so-called *mini-disks* (see, for instance, Hayasaki et al. 2007; Farris et al. 2012, 2014; Gold et al. 2014; Bowen et al. 2017, 2018, 2019; Moody et al. 2019; Muñoz et al. 2019, 2020). If the binary separation is more than a few tens of M, where we use geometrical units and M is the mass of the system, accretion of each mini-disk is slow because it is limited by internal angular momentum transport. However, at smaller binary separations, the ratio between the radius of each minidisk's outer edge and its ISCO shrinks to be only order unity; in that situation, the need for angular momentum transport diminishes, and their mass content becomes far more time-variable (Bowen et al. 2017, 2018, 2019). Efforts toward producing realistic spectra from these simulations have begun (d'Ascoli et al. 2018).

The techniques used to achieve these results are highly diverse, but a key feature of the system has remained elusive: the spin of the BHs. In fact, most of these works assume Newtonian gravity, while black hole spin is inherently relativistic. Although some works evolved the full set of Einstein Field Equations (EFE) for the metric of the spacetime and matter fields (Bode et al. 2011; Farris et al. 2011; Giacomazzo et al. 2012; Gold et al. 2014), they focused on binaries close to merger ($b \leqslant 10M$), where the strong tidal interactions and short inspiral timescale prevent the formation of mini-disks. An intermediate strategy in modeling the gravitational field has been to employ an approximate metric for the background spacetime, still capturing the relativistic nature of the system while being freed from the computational load of integrating the EFE. For instance, Noble et al. (2012) excised the inner region and used a Post-Newtonian (PN) metric of order 2.5-PN to integrate the equations of general relativistic magnetohydrodynamics (GRMHD) in the circumbinary region. Bowen et al. (2017, 2018, 2019) used the global approximate metric of Mundim et al. (2014) to explore the relativistic dynamics of the mini-disks in non-spinning binaries. The approach of Mundim et al. (2014) for building the approximate spacetime can be generalized to spinning binaries (Gallouin et al. 2012; Ireland et al. 2016), but the analytical metric becomes too complex and computationally expensive for GRMHD simulations.

In this work, we perform the first simulations of this system including spin. To do so, we construct a new approximate metric for the spacetime of a pair of spinning black holes by linearly superimposing two individual BHs in the Kerr–Schild gauge. This new metric, which we call Superposed Kerr–Schild (SKS), presents many advantages over our previous approach. It is well-behaved in every region of spacetime, it is easy to implement, it is computationally efficient, and it permits easy inclusion of spin. Using this approximate spacetime, we have been able to conduct lengthy GRMHD simulations of circumbinary accretion onto a SMBBH whose black holes spin.

Our work is organized as follows. In Section 2 we introduce the Kerr–Schild gauge and construct the SKS metric for the BBH spacetime. In Section 3 we analyze the validity of the SKS metric as a solution of EFE in vacuum. Then, in Section 4, we describe the configurations of our GRMHD simulations of circumbinary disks around spinning binaries. Section 5 is devoted to our main results on the effects of the spins on the properties of the evolved circumbinary disks. Finally, in Section 6, we summarize our main conclusions. Throughout this paper, Latin indices denote spatial indices, running from 1 to 3; Greek indices denote spacetime indices, running from 0 to 3 (0 is the time coordinate); and the Einstein summation convention is used. We work on geometrical units where $G = c = 1$, and the total mass of the binary M is normalized to unity.

2. Spacetime Construction

2.1. Kerr–Schild Form for Single Black Holes

The Kerr–Schild form of the metric for the spacetime of a single, rotating, black hole is (see the republication Kerr & Schild 2009)

$$g_{\mu\nu} = \eta_{\mu\nu} + 2\mathcal{H}l_\mu l_\nu, \tag{1}$$

where, in Kerr–Schild Cartesian coordinates $x^\alpha = (t, x, y, z)$, $\eta_{\mu\nu} = \mathrm{diag}(-1, 1, 1, 1)$, l_μ denotes a null vector with respect to both metrics $g^{\mu\nu}l_\mu l_\nu = \eta^{\mu\nu}l_\mu l_\nu = 0$, and $\mathcal{H}$ is a scalar function of coordinates. These read:

$$l_\mu = \left(1, \frac{r_{\mathrm{KS}}x + ay}{r_{\mathrm{KS}}^2 + a^2}, \frac{r_{\mathrm{KS}}y - ax}{r_{\mathrm{KS}}^2 + a^2}, \frac{z}{r_{\mathrm{KS}}}\right), \tag{2}$$

$$\mathcal{H} = \frac{Mr_{\mathrm{KS}}}{r_{\mathrm{KS}}^2 + a^2\cos^2\theta}, \tag{3}$$

with the auxiliary functions

$$r_{\mathrm{KS}}^2 = \frac{1}{2}(\rho^2 - a^2) + \sqrt{\frac{1}{4}(\rho^2 - a^2)^2 + a^2 z^2}, \tag{4}$$

$$\rho^2 = x^2 + y^2 + z^2, \tag{5}$$

$$\cos\theta = \frac{z}{r_{\mathrm{KS}}}, \tag{6}$$

being M the Arnowitt–Deser–Misner (ADM) mass of the black hole, and a its specific angular momentum.

Kerr–Schild coordinates are widely used for their computational advantages. The coordinates x^α are horizon-penetrating, and singular regions are contained within the event horizon. This allows the excision of singularities from the computational domain while keeping the physics at the exterior of the black hole unaffected. Furthermore, the Kerr–Schild form is invariant under a Lorentz-boost transformation:

$$\bar{x}^\alpha = \Lambda^\alpha{}_\beta x^\beta, \tag{7}$$

$$\bar{\mathcal{H}}(\bar{x}^\alpha) = \mathcal{H}([\Lambda^{-1}]^\alpha{}_\beta \bar{x}^\beta), \tag{8}$$

$$\bar{l}_\mu(\bar{x}^\alpha) = \Lambda^\nu{}_\mu l_\nu([\Lambda^{-1}]^\alpha{}_\beta \bar{x}^\beta), \tag{9}$$

where $\Lambda^\alpha{}_\beta$ are the components of the usual Lorentz matrix for uniform velocity v^i. The resulting metric represents the spacetime of a moving, rotating, black hole.

The invariance of the Kerr–Schild form under boosts is useful for approximating the spacetime of multiple moving black holes by linearly superposing terms of the form $2\mathcal{H}^{(n)}l_\mu^{(n)}l_\nu^{(n)}$ to the same asymptotic background $\eta_{\mu\nu}$, where $n = 1, 2, \ldots$ accounts for each black hole, with mass $M^{(n)}$ and specific angular momentum $a^{(n)}$.

2.2. SKS as Initial Data for Black Hole Binaries

As mentioned in Section 1, our approach for evolving the spacetime of spinning BBHs is to construct an approximate metric based on the superposition of two Kerr–Schild black holes. In this subsection, we briefly review how an equivalent superposition has been used for setting initial data (ID) in Numerical Relativity simulations, i.e., simulations that evolve EFE for the spacetime metric (see Duez & Zlochower 2018, for a review). Indeed, in the context of Numerical Relativity, one needs a valid set of ID that solves the constraints of EFE at some Cauchy surface. The standard case, where one solves the initial metric for a given distribution of matter, presents the problem of having to determine 12 degrees of freedom from just 4 equations Cook (2000). Some techniques have been proposed for fixing free degrees of freedom in advance, while simplifying the constraint equations.

For instance, the conformal-transverse-traceless (CTT) decomposition (York 1971; Bowen & York 1980) asks for a conformally related spatial metric $\tilde{\gamma}_{ij}$, and the trace and conformal traceless part of the extrinsic curvature, before solving the remaining 4 degrees of freedom, contained in the conformal factor ψ, and potential functions W^i. This technique is particularly convenient for conformally flat spacetimes, where the resulting equations simplify significantly, but BBH spacetimes are not conformally flat (Damour et al. 2000) and this technique possesses some limitations. For instance, it is not possible to construct ID for BBHs with spins larger than ∼0.93 from a conformally flat approach (Dain et al. 2002; Lousto et al. 2012).

An alternative prescription for the conformal metric $\tilde{\gamma}_{ij}$ was introduced by Matzner et al. (1998), based on the linear superposition of two boosted Kerr–Schild black holes:

$$\tilde{\gamma}_{ij} = \delta_{ij} + 2\bar{\mathcal{H}}^{(1)}\bar{l}_i^{(1)}\bar{l}_j^{(1)} + 2\bar{\mathcal{H}}^{(2)}\bar{l}_i^{(2)}\bar{l}_j^{(2)}. \qquad (10)$$

Using this approach, Marronetti et al. (2000) and Marronetti & Matzner (2000) solved the resulting constraint equations for ψ and W^i and found that the solution was in good agreement with the conformal ansatz (10), even for close separations (∼10M). Additionally, Bonning et al. (2003) supported this claim, and demonstrated that this proposal is well suited for capturing the physics of the BBH inspiral as it contains the right Newtonian binding energy for wide separations ($b > 15M$). More recently, Lovelace et al. (2008, 2012), Scheel et al. (2015), Healy et al. (2016), Ruchlin et al. (2017), Zlochower et al. (2017) used the

superposition of conformally Kerr–Schild black holes to develop new ID that can be used to evolve BBH with spins as high as 0.994. We conclude that, although some junk gravitational radiation might be present (Pfeiffer et al. 2002), the ansatz (10) approximates the spacetime of widely separated BHs at a given time.

2.3. Time-dependent SKS for Binary Black Hole Evolution

Motivated by the success of the superimposed prescription (10) as ID, we model the four-dimensional spacetime of a BBH system with a superimposition of two boosted Kerr–Schild black holes, updating the position and velocity of each black hole for a given trajectory. We call this metric SKS and reads:

$$g_{\mu\nu} = \eta_{\mu\nu} + 2\hat{\mathcal{H}}^{(1)}\hat{l}_\mu^{(1)}\hat{l}_\nu^{(1)} + 2\hat{\mathcal{H}}^{(2)}\hat{l}_\mu^{(2)}\hat{l}_\nu^{(2)}, \qquad (11)$$

where

$$\hat{x}^{(n)\alpha} = \Lambda_{\text{circ}}^{(n)}(x^\alpha), \qquad (12)$$

$$\hat{\mathcal{H}}^{(n)}(\hat{x}^{(n)\alpha}) = \mathcal{H}^{(n)}[\Lambda_{\text{circ}}^{(n)\,-1}(\hat{x}^\alpha)], \qquad (13)$$

$$\hat{l}_\mu^{(n)}(\hat{x}^{(n)\alpha}) = \Lambda^{(n)\nu}{}_\mu l_\nu^{(n)}[\Lambda_{\text{circ}}^{(n)\,-1}(\hat{x}^\alpha)]. \qquad (14)$$

We apply standard Lorentz transformations $\Lambda^{(n)}$ to vector fields $l^{(n)}$, so we keep an inertial frame $\eta_{\mu\nu}$ at infinity, but we apply a nonlinear transformation $\Lambda_{\text{circ}}^{(n)}$ to coordinates in order to force the BHs to move on the desired trajectory. We call this last transformation *circular boost* and we introduce it below.

Each black hole is boosted with a different velocity $v^{(n)i}$, updated as a function of time to be the tangential velocity of a given orbit. In a first approximation, we consider equal-mass black holes, and Keplerian circular trajectories in the x–y plane, with separation b:

$$x_{\text{K}}^{(1)} = \frac{b}{2}\cos(\phi), \;\; y_{\text{K}}^{(1)} = \frac{b}{2}\sin(\phi), \;\; z_{\text{K}}^{(1)} = 0, \qquad (15)$$

$$x_{\text{K}}^{(2)} = -\frac{b}{2}\cos(\phi), \;\; y_{\text{K}}^{(1)} = -\frac{b}{2}\sin(\phi), \;\; z_{\text{K}}^{(2)} = 0, \qquad (16)$$

where $\phi = \Omega t$, and

$$\Omega = \sqrt{\frac{M^{(1)} + M^{(2)}}{b^3}}. \qquad (17)$$

The time-dependent velocities are derived by $v^{(n)i} = dx_{\text{K}}^{(n)i}/dt$.

The nonlinear transformation $\Lambda_{\text{circ}}^{(n)}$ is constructed as follows: A standard boost of coordinates $\Lambda^{(n)}$ results on the BH moving on a straight line, with uniform velocity v^i. This is encoded on time-dependent terms of the form $v^i t$ in the transformation. Here, we replace such terms with the trajectories $(x_{\text{K}}^{(n)}, y_{\text{K}}^{(n)}, z_{\text{K}}^{(n)})$ given by Equations (15) and (16). The transformation reads:

$$\Lambda_{\text{circ}}^{(n)\,-1}(\hat{x}^\alpha) = \begin{bmatrix} \gamma^{(n)}\hat{t} - \gamma^{(n)}\breve{v}^{(n)x}\hat{x} - \gamma^{(n)}\breve{v}^{(n)y}\hat{y} \\ -x_{\text{K}}^{(n)} + [1 + (\gamma^{(n)} - 1)(\breve{v}^{(n)x})^2]\hat{x} + [(\gamma^{(n)} - 1)\breve{v}^{(n)x}\breve{v}^{(n)y}]\hat{y} \\ -y_{\text{K}}^{(n)} + [(\gamma^{(n)} - 1)\breve{v}^{(n)y}\breve{v}^{(n)x}]\hat{x} + [1 + (\gamma^{(n)} - 1)(\breve{v}^{(n)y})^2]\hat{y} \\ \hat{z} \end{bmatrix}, \qquad (18)$$

where $\check{v}^{(n)i} = v^{(n)i}/|v^{(n)}|$ are the normalized components of the boost velocities. The transformation $\Lambda_{\mathrm{circ}}^{(n)}$ is nonlinear in the sense that it cannot be written as the linear product of a matrix and the coordinates $\hat{x}^{\mu}$. However, its expansion for short intervals of time reduces to a standard boost $\Lambda^{(n)-1}$ to the rest frame of the BH, followed by a solid translation to the BH center.

3. Spacetime Validation

The SKS metric represents an approximate vacuum solution of EFE. Therefore, it should approximately satisfy $R_{\mu\nu} = 0$, where $R_{\mu\nu}$ is the Ricci tensor. To quantify deviations from a vacuum solution, following Mundim et al. (2014), we calculate and analyze the Ricci scalar $R := R_{\mu\nu}g^{\mu\nu}$ for the SKS metric.

Even though the metric is analytical, we compute the required derivatives numerically. We include the SKS metric (11) in a stand-alone code that builds a uniform, three-dimensional, Cartesian grid, and computes the required first and second-order derivatives by fourth-order finite differences. We evaluate the metric components at the corners of the Cartesian cells since these positions are shared by different resolutions and this is useful for later convergence analysis.

In Figure 1, we plot the resulting values of the Ricci scalar R at $t = 0$ in the plane of the BHs, for different spatial scales, and spin values. We study the case of equal-mass BHs $M^{(1,2)} = 0.5M$, separated by $b = 20M$. The top row shows the results for a grid centered at the center of mass of the system. For coordinates (x, y, z) the domain dimensions are $(160, 160, 40)M$, and there are $320 \times 320 \times 80$ cells. In the left, middle, and right columns, the BH spins are $-0.9M^{(1,2)}$, 0 and $0.9M^{(1,2)}$, respectively. Within the circumbinary region, the violations of $R = 0$ are comparable to those of Mundim et al. (2014), and this result is independent of spin for the three cases we explored.

In the middle row of Figure 1, we focus on the orbital region by reducing the grid dimensions to $(40, 40, 10)M$ while keeping the same number of cells. In the domain of the binary $(r < b/2)$, particularly between the BHs, the quality of the spacetime is not as good as in the circumbinary region, but the values of R are still comparable to those of Mundim et al. (2014). The bottom row shows the Ricci scalar R for grid lengths of $(5, 5, 1.25)M$, centered on one of the BHs, while keeping the same number of cells. We notice the metric captures the singularities of spinning BHs.

Convergence testing proves that the numerical calculation of the Ricci scalar R converges to the analytical value. To that end, we recalculate the Ricci scalar for the region of the middle row of Figure 1 with successively coarser resolutions: $160 \times 160 \times 40$ and $80 \times 80 \times 20$. Then we calculate the local convergence factor,

$$p_R = \frac{1}{\log 2}\log\left|\frac{R_{\Delta_0} - R_{\Delta_1}}{R_{\Delta_1} - R_{\Delta_2}}\right|, \qquad (19)$$

where R_{Δ_0}, R_{Δ_1} and R_{Δ_2} are, respectively, the values of R for the coarsest, middle, and finest resolutions, computed at the corners of the coarsest grid cells because these positions are shared by the three resolutions. Figure 2 shows these values of p_R in the BH orbital plane; throughout this region $p_R \approx 4$, as expected from a fourth-order finite differencing scheme. The apparent non-convergence in the regions close to the BHs is because the coarsest grid fails to resolve such high curvatures.

In this section we analyzed the Ricci scalar R for the SKS metric and find it is approximately zero, as expected for a vacuum solution of EFE. The accuracy of this four-dimensional scalar allows us to use the SKS metric as a time-dependent geometry for the background spacetime in GRMHD simulations. Though not included in this article, we also checked for the Hamiltonian and momentum constraints, and found them to be satisfied to the same degree of accuracy as the Ricci scalar R. As a further validation test, in Appendix B we prove the expansion of this metric agrees with the lowest PN expansion of the metric of spinning binaries.

4. Circumbinary Disk Models

As a first application of the SKS metric (11), we build and evolve a torus of gas in the circumbinary region. We evolve the system integrating the GRMHD equations of motion (EoM) with the well-tested code HARM3D (Gammie et al. 2003; Noble et al. 2006, 2009). We neglect the contribution of matter fields to spacetime curvature and use the SKS metric as the background geometry. Since we focus on the features of the circumbinary disk, we excise a spherical region at the center of the domain that contains the BHs.

4.1. GRMHD Evolution

The evolution of the circumbinary disk follows from the integration of the GRMHD EoM on the background SKS metric. These equations are the continuity equation, the local conservation of energy and momentum, and Maxwell's equations (see Noble et al. 2009). In flux-conservative form, these read:

$$\partial_t U(P) = -\partial_i F^i + S(P), \qquad (20)$$

where P is the vector of *primitive* variables, U the vector of *conserved* variables, F the *fluxes*, and S the *sources*. They read:

$$P = [\rho, P, \tilde{u}^k, B^k]^{\mathrm{T}}, \qquad (21)$$

$$U(P) = \sqrt{-g}\,[\rho u^t, T^t{}_t + \rho u^t, T^t{}_j, B^k]^{\mathrm{T}}, \qquad (22)$$

$$F^i(P) = \sqrt{-g}\,[\rho u^i, T^i{}_t + \rho u^i, T^i{}_j, (b^i u^k - b^k u^i)]^{\mathrm{T}}, \qquad (23)$$

$$S(P) = \sqrt{-g}\,[0, T^\kappa{}_\lambda \Gamma^\lambda{}_{t\kappa} - \mathcal{F}_t, T^\kappa{}_\lambda \Gamma^\lambda{}_{j\kappa} - \mathcal{F}_j, 0^k]^{\mathrm{T}}, \qquad (24)$$

where g denotes the determinant of the SKS metric, ρ is the rest mass density, u^μ is the fluid four-velocity, and $\tilde{u}^\mu$ is the fluid four-velocity as measured by a zero angular momentum observer (ZAMO). The magnetic field is represented by $B^k = {}^*F^{kt}\sqrt{4\pi}$, where ${}^*F^{\mu\nu}$ is the dual of the Maxwell tensor, $b^\mu = (\delta^\mu_\nu + u^\mu u_\nu)B^\nu$ is the projection of the magnetic field into the fluid's comoving frame. In addition, $\Gamma^\lambda{}_{\mu\nu}$ is the affine connection for the SKS metric and $T^\mu{}_\nu$ is the sum of the stress-energy tensor of a perfect fluid and the EM stress-energy tensor, defined as:

$$T_{\mu\nu} = (\rho h + 2p_{\mathrm{m}})u_\mu u_\nu + (p + p_{\mathrm{m}})g_{\mu\nu} - b_\mu b_\nu, \qquad (25)$$

where p denotes the pressure of the fluid, $h = 1 + \epsilon + p/\rho$ the specific enthalpy, ϵ the specific internal energy, and $p_{\mathrm{m}} = b^\mu b_\mu/2$ the magnetic pressure. The internal energy is $u = \rho\epsilon$, and we assume an adiabatic Γ-law equation of state: $P = (\Gamma - 1)u$, with $\Gamma = 5/3$, corresponding to a non-relativistic fluid without internal degrees of freedom.
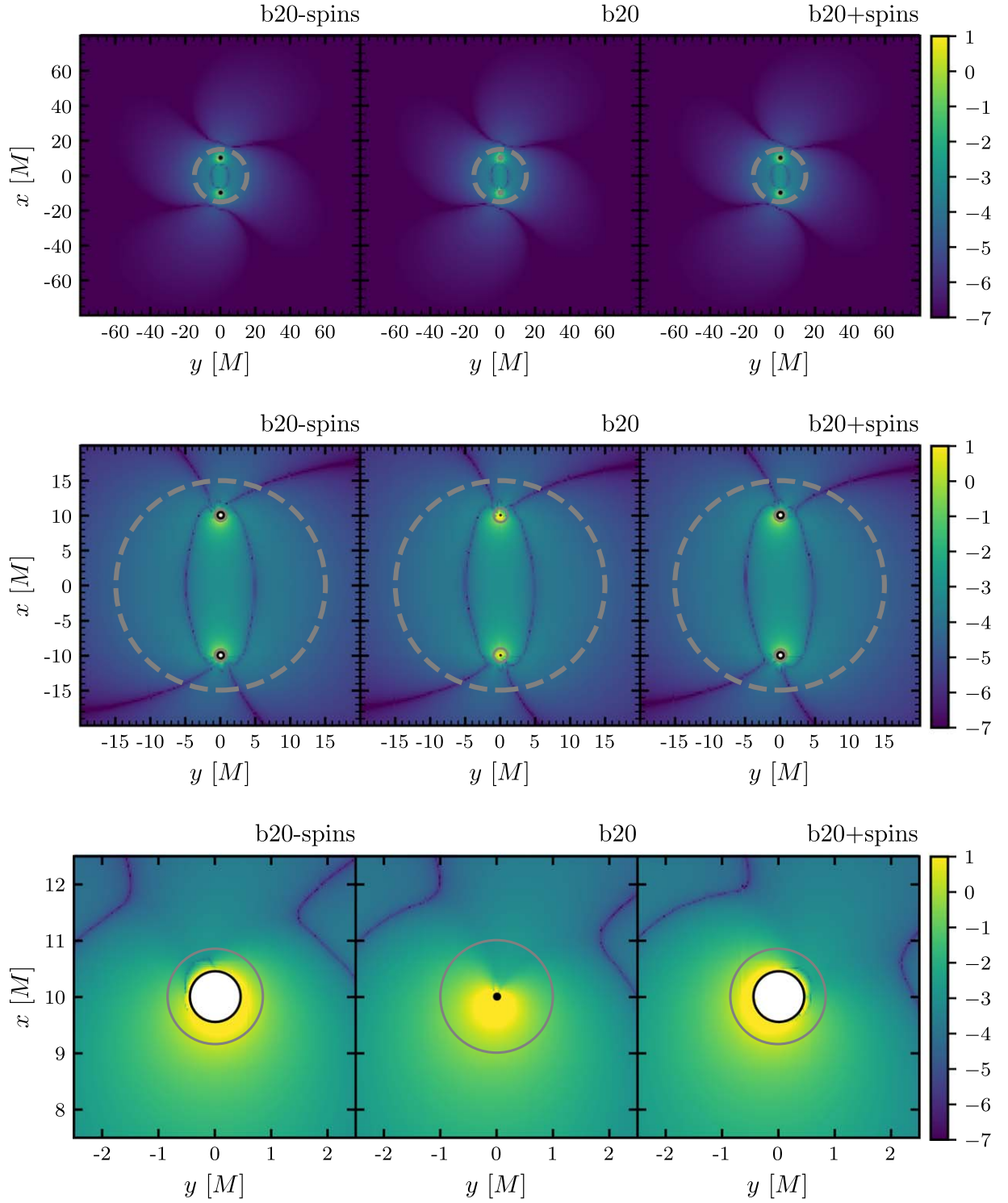
Figure 1. Ricci scalar at the equator for the SKS metric for anti-aligned spins (left), non-spinning (center), and aligned spins (right), at different scales (top, center, bottom). Solid-gray circles estimate the BHs horizons at $r^{(1,2)2} = 2M^{(1,2)}(M^{(1,2)} + \sqrt{M^{(1,2)2} - a^{(1,2)2}})$, solid-black circles estimate the BHs singular regions at $r^{(1,2)} = |a^{(1,2)}|$, where $r^{(n)}$ is the radial distance from the nth BH. These estimations follow from known singularities and horizons for a single BH in Cartesian-KS coordinates. Dashed circles represent the limit of the excised region of the domain of our GRMHD simulations, at $r = 15M$. The Ricci scalar is calculated through 4th-order finite differencing of the SKS metric (11), in Cartesian-KS coordinates, with $320 \times 320 \times 80$ cells, for grid lengths of (160, 160, 40) (top), (40, 40, 10) (center), and (5, 5, 1.25) (bottom), respectively, for x, y, z.

In accretion disks, dissipation converts magnetic and kinetic turbulence into heat. To regulate the consequent growth in the temperature, we follow Noble et al. (2009) and include a sink term $\mathcal{F}^\mu$ in the conservation Equations (20). This term portrays the effect of optically thin radiative cooling. For isotropic emission in the fluid's frame, the sink term takes the form $\mathcal{F}_\nu = \mathcal{L}_{\rm cool} u_\nu$, where $\mathcal{L}_{\rm cool}$ is the *cooling function*, defined as the rate of radiated energy per unit of proper time. We set $\mathcal{L}_{\rm cool}$
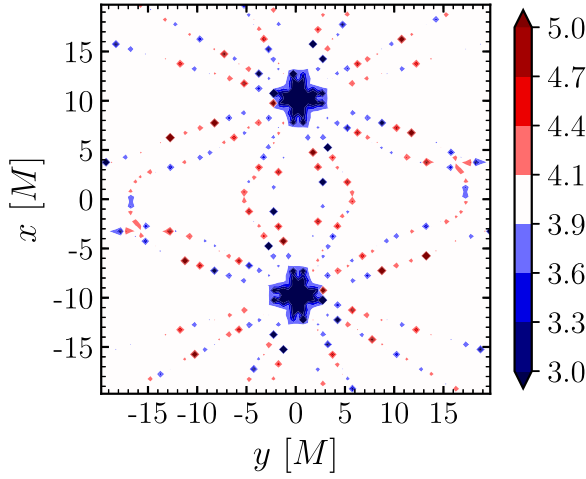
Figure 2. Convergence factor p_R (Equation (19)) in linear colorscale, measured in the BH orbital plane, as determined from resolutions: $\Delta_1 x = 0.5$, $\Delta_2 x = 0.25$, $\Delta_3 x = 0.125$.

to follow the local increase in entropy S, cooling the plasma to the initial entropy S_0 (Noble et al. 2012):

$$\mathcal{L}_{\text{cool}} = \frac{\rho \epsilon}{t_{\text{cool}}} \left(\frac{\Delta S}{S_0} + \left| \frac{\Delta S}{S_0} \right| \right)^{1/2}, \qquad (26)$$

where $\Delta S = S - S_0$, $S = p/\rho^\Gamma$, $S_0 = 0.01$, and $t_{\text{cool}} = 2\pi(r/M)^{3/2}$. We do not cool unbound material, defined as the portion of the plasma where $(\rho h + 2p_m)u_t < -\rho$. By controlling the temperature, the cooling function stabilizes the aspect ratio H/r of the disk (see Equation (A3)); at the same time, it also estimates the luminosity. Noble et al. (2012) did not claim to include the square root in Equation (26), but this is a typo in the manuscript and the square root was actually included in the computational code (personal communication).

We integrate the conservation Equations (20) with high-resolution shock-capturing schemes implemented in HARM3D (Gammie et al. 2003; Noble et al. 2006, 2009). After reconstruction of the primitive variables to the cell interfaces through a piecewise parabolic method, we apply the Lax-Friedrichs formula to compute the local fluxes (Gammie et al. 2003). We use fourth-order finite differences for spatial derivatives, and the method of lines for time integration with a Runge–Kutta method of second-order. If the updates of ρ or u go below the corresponding atmosphere values $\rho_{\text{atm}} = 2 \times 10^{-10}(r/M)^{-3/2}$, $u_{\text{atm}} = 2 \times 10^{-12}(r/M)^{-5/2}$ they are reset to the latter. The primitive variables are recovered from the conserved variables with the scheme described in Noble et al. (2006). We use the constrained transport (FluxCT) algorithm (Toth 2000) to maintain the solenoidal constraint, $\partial_i(\sqrt{-g}\, B^i) = 0$. For more details on the numerical implementation, see Noble et al. (2009).

4.2. Circumbinary Disk Initialization

As initial data for the matter fields, we construct a torus in nearly hydrostatic equilibrium at the circumbinary region. Fishbone & Moncrief (1976) and Chakrabarti (1985) presented this solution to the relativistic Euler's equations for the case of stationary and axisymmetric spacetimes in Boyer–Lindquist (BL) coordinates, where the only non-zero off-diagonal components of the metric are $g_{t\phi}^{\text{BL}}$ and $g_{\phi t}^{\text{BL}}$. To use the same technique and build the torus on the stationary and axisymmetric spacetime, we

transform the SKS metric (11) to BL-like coordinates and take a ϕ-average of the metric as we explain below.

First, we transform the whole SKS metric (11) from Cartesian-KS to BL-like coordinates using the standard transformations for a single, non-spinning black hole with mass $M = M^{(1)} + M^{(2)}$. The transformation is given by:

$$t = u_{\text{BL}} - r_{\text{BL}} + \int dr_{\text{BL}} \frac{r_{\text{BL}}}{r_{\text{BL}} - 2M}, \qquad (27)$$

$$x_{\text{KS}} = r_{\text{BL}} \sin\theta_{\text{BL}} \cos\phi_{\text{BL}}, \qquad (28)$$

$$y_{\text{KS}} = r_{\text{BL}} \sin\theta_{\text{BL}} \sin\phi_{\text{BL}}, \qquad (29)$$

$$z_{\text{KS}} = r_{\text{BL}} \cos\theta_{\text{BL}} \qquad (30)$$

The metric transforms in the usual way:

$$g_{\mu\nu}^{\text{BL}} = \frac{dx_{\text{KS}}^\alpha}{dx_{\text{BL}}^\mu} \frac{dx_{\text{KS}}^\beta}{dx_{\text{BL}}^\nu} g_{\alpha\beta}^{\text{KS}}. \qquad (31)$$

The SKS spacetime has a helical Killing symmetry through the Killing vector $\mathcal{K}^\mu = (\partial_t)^\mu + \Omega_{\text{bin}}(\partial_\phi)^\mu$, where Ω_{bin} is the binary orbital frequency, and the time average of the metric coincides with the corresponding azimuthal average. Then, following the procedure of Noble et al. (2012), we construct a stationary and axisymmetric spacetime from the azimuthal average:

$$\tilde{g}_{\mu\nu}^{\text{BL}} = \frac{\int g_{\mu\nu}^{\text{BL}} \sqrt{g_{\phi\phi}^{\text{BL}}}\, d\phi}{\int \sqrt{g_{\phi\phi}^{\text{BL}}}\, d\phi}. \qquad (32)$$

We then follow the steps of Noble et al. (2012) for the construction of the torus over the metric (32). The free parameters of this model are the radial distance to the disk inner edge r_{in}, the radial distance to the maximum of pressure r_p, and the specific angular momentum of the fluid at the inner edge l_{in}. From such a procedure, we obtain the hydrodynamic properties of the fluid, including its four-velocity in BL coordinates u_{BL}^μ. Transforming the four-velocity to Cartesian-KS via $u_{\text{KS}}^\mu = \frac{dx_{\text{KS}}^\mu}{dx_{\text{BL}}^\alpha} u_{\text{BL}}^\alpha$, we obtain the hydrodynamical ID for the torus in a coordinate system consistent with the SKS metric (11). We include random perturbations of the internal energy $u = \rho\epsilon$, with amplitude 10^{-2}, to precipitate turbulence and accretion.

We initialize the magnetic field in the interior of the disk as a set of dipolar loops that follow the lines of constant density of the fluid. The corresponding vector potential A_μ in spherical coordinates (t, r, θ, ϕ) has one non-vanishing component:

$$A_\phi = A_0 \max[(\rho - \rho_{\text{cut}}), 0], \qquad (33)$$

where $\rho_{\text{cut}} = 0.25\, \rho_{\text{max}}$ so the initial magnetic field is entirely confined within the torus and the field lines wrap around the region of maximum density ρ_{max}. The constant A_0 is chosen such that the initial ratio of the fluid integrated pressure to the magnetic integrated pressure satisfies:

$$\frac{\int p \sqrt{-g}\, d^3 x}{\int p_m \sqrt{-g}\, d^3 x} \sim 100. \qquad (34)$$

In this way, the initial equilibrium between thermal and magnetic stresses is comparable for different simulations. In the next subsection, we explain how these spherical coordinates (t, r, θ, ϕ) relate to the Cartesian-KS. Noble et al. (2012) claimed that the ratio of the fluid's total internal energy to the total magnetic energy was initialized to 100, but this is a typo

in the manuscript and actually the condition (34) was demand (personal communication).

We fill the region outside the torus with an atmosphere, or numerical vacuum, modeled by a tenuous, non-magnetized, static fluid in approximate hydrostatic equilibrium: $\rho_{\rm atm} = 2 \times 10^{-10}(r/M)^{-3/2}$, $u_{\rm atm} = 2 \times 10^{-12}(r/M)^{-5/2}$, and $u^i_{\rm atm} = 0$.

The last step of the initialization involves the transformation of the SKS metric (11), the initial four-velocity $u^\mu_{\rm KS}$, and the initial four-vector potential A_μ, to the numerical coordinates used for the integration of the GRMHD EoM (see the next subsection).

4.3. Numerical Grid, Boundary Conditions, and Simulation Parameters

Numerical errors in conservation of momentum are smallest in the direction of coordinate lines; consequently, given the approximate axisymmetry of the system, the Cartesian-KS basis would be a poor choice for the global coordinates of the simulation. We move to a spherical basis through a standard spatial transformation:

$$t = t, \tag{35}$$
$$x_{\rm KS} = r\sin\theta\cos\phi, \tag{36}$$
$$y_{\rm KS} = r\sin\theta\sin\phi, \tag{37}$$
$$z_{\rm KS} = r\cos\theta. \tag{38}$$

These are the physical coordinates in our simulation.[10]

For the actual integration of the EoM we move to a numerical coordinate system $(x^{(0)}, x^{(1)}, x^{(2)}, x^{(3)})$ that relates to the physical one by:

$$t = x^{(0)}, \tag{39}$$
$$r(x^{(1)}) = Me^{x^{(1)}}, \tag{40}$$
$$\theta(x^{(2)}) = \frac{\pi}{2}[1 + (1 - \xi)(2x^{(2)} - 1) +$$
$$+ \left(\xi - \frac{2\theta_c}{\pi}\right)(2x^{(2)} - 1)^n] \tag{41}$$
$$\phi(x^{(3)}) = x^{(3)}, \tag{42}$$

where $n = 9$, $\xi = 0.87$, and $\theta_c = 0.2$. We construct a uniform grid of $(x^{(1)}, x^{(2)}, x^{(3)})$ where the center of the i, j, k-cell has coordinates $(x_i^{(1)}, x_j^{(2)}, x_k^{(3)})$, with $x_i^{(1)} = x_{\rm b}^{(1)} + (i + 1/2)\Delta x^{(n)}$, and equivalently for $x_j^{(2)}$ and $x_k^{(3)}$. The grid, then, is determined by the parameters: $x_{\rm b}^{(1)} = \ln(r_{\rm min}/M)$, $\Delta x^{(1)} = \ln(r_{\rm max}/r_{\rm min})/N^{(1)}$, $r_{\rm min} = 15M$, $r_{\rm max} = 300M$, $N^{(1)} = 300$, $x_{\rm b}^{(2)} = 0$, $\Delta x^{(2)} = 1/N^{(2)}$, $N^{(2)} = 160$, $x_{\rm b}^{(3)} = 0$, $\Delta x^{(3)} = 2\pi/N^{(3)}$, and $N^{(3)} = 400$. A uniform grid of these numerical coordinates implies better resolution at smaller physical radii and at the equatorial plane of the system. Noble et al. (2012) showed that, in these conditions, this grid resolves the magnetorotational instability (MRI) (Velikhov 1959; Chandrasekhar 1960; Balbus & Hawley 1991) and spiral density waves generated by the binary torques.[11] We evolve this system

---

[10] These coordinates are not the usual spherical Kerr–Schild coordinates used in the literature of accretion disks (see, for instance, Gammie et al. 2003), but they result from a standard spherical transformation of the Cartesian Kerr–Schild coordinates usually used in the literature of Numerical Relativity (see, for instance, Matzner et al. 1998).

[11] There is a small difference between our grid and the one used by Noble et al. (2012). The latter set $r_{\rm max} = 260M$, but we extend it to $r_{\rm max} = 300M$. Our grid still satisfies the physical resolution requirements.

from $t = 0$ to $t = 1.5 \times 10^5 M$, using a dynamical step $\Delta t = 0.45\Delta t_{\rm min}$, where $\Delta t_{\rm min}$ is the shortest cell crossing time of matter fields over the domain at each time.

Boundary conditions are imposed through zeroth-order extrapolation of primitive variables into ghost zones. Specifically, outflow boundary conditions are applied on $x^{(1)}$ and $x^{(2)}$-boundaries, while periodic boundary conditions are used on $x^{(3)}$-boundaries. We force $u^r = 0$ if it points into the domain at the r-boundaries. This diode-type condition was found to be unstable in some circumstances involving low-density regions by Noble et al. (2012) but successfully used in Newtonian simulations by MacFadyen & Milosavljević (2008), Shi et al. (2012), D'Orazio et al. (2013), among others.

We perform a set of five runs, denoted: `b20-spins`, `b20_v0`, `b20_v1`, `b20_v2`, `b20+spins`. In every run, the BHs have equal masses: $M^{(1)} = M^{(2)} = 0.5$, so the total mass of the system is $M = 1$; the distance between them is fixed to $b = 20M$. The disk's initial inner edge is at $r_{\rm in} = 60M$, and the initial pressure maximum is at $r_{\rm p} = 100M$.

The spins of the BHs in `b20-spins` are $a^{(1)} = a^{(2)} = -0.9M^{(1,2)}$, i.e., opposite to the angular momentum of the binary. The spins in run `b20+spins` have the same magnitude but are aligned with the orbital angular momentum. Runs `b20_v0`, `b20_v1`, `b20_v2` have no spin. These three runs differ from one another only in the random initial perturbations of the internal energy; the goal of these runs is to calibrate the size of intrinsic fluctuations due to turbulence so that we can tell whether the spin runs differ significantly. In Table 1 we gather the relevant properties of the binaries and initial disks of our runs.

The specific angular momentum of the fluid at the inner edge of the disk $l_{\rm in}$ is set so the ratio H/r equals 0.1 at $r_{\rm p}$. This results in $l_{\rm in} = 8.62M$, $8.60M$, $8.60M$, $8.60M$ and $8.57M$ for `b20-spins`, `b20_v0`, `b20_v1`, `b20_v2` and `b20+spins`, respectively (see Table 1).

5. Circumbinary Disk Dynamics

To globally characterize the dynamics of these simulations, in Figure 3 we plot the accretion rate $\dot{M}$ as a function of time (see Equation (A4)) at the innermost radial boundary of the domain. We distinguish three dynamical stages in this plot: MRI growth ($t = 0–30 \times 10^3 M$), in which the MRI grows to its saturated amplitude; subsequent relaxation ($t = 30–75 \times 10^3 M$), in which the accretion rate progressively diminishes over time; and a steady state ($t = 75–150 \times 10^3 M$). The first is a transient period, and will not be included in our analysis. The second stage is still affected by the initial transient and will not be used for our main conclusions. We will focus, instead, on the steady state epoch.

We organize our results in three subsections. First, we focus on the properties of the plasma that are sensitive to the spins; these properties are mostly related to the cavity and the accretion streams. Then, in the second subsection, we interpret these spin-sensitive results in terms of the gravitational potential of the linearized SKS metric. Finally, in the third subsection, we describe the bulk properties of the circumbinary disk, all of them insensitive to the spin of the BHs.

Because MHD turbulence is a fundamental property of accretion disks, all our results are subject to intrinsic variance. This fact complicates the identification of subtle physical processes such as the effect of the spins on the circumbinary disk. To quantify this variance, we use the subset of runs `b20_v0`, `b20_v1`, and `b20_v2`. The parameters of these three
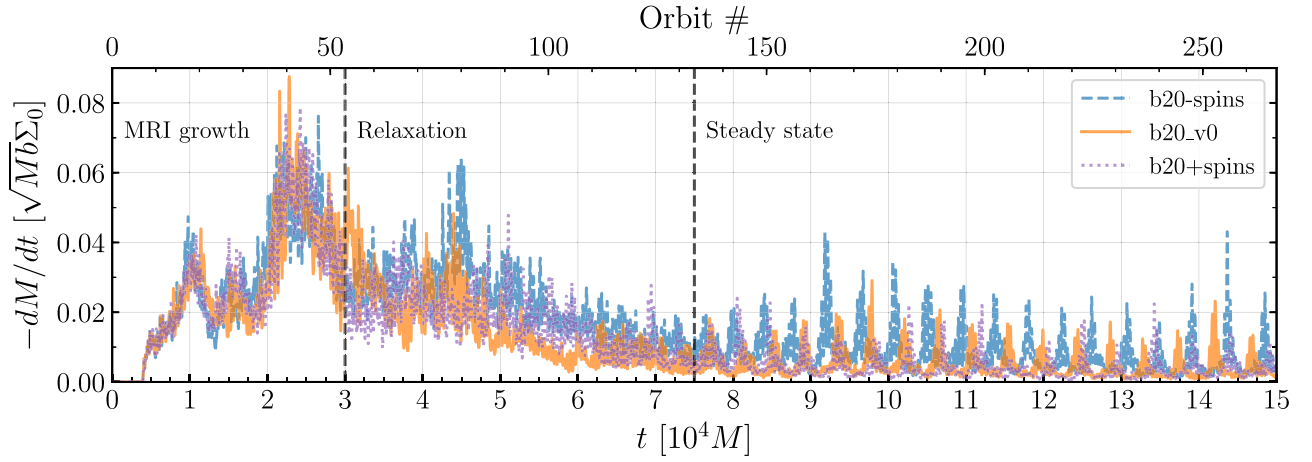
Figure 3. Accretion rate integrated at the innermost boundary of the grid, as a function of time. From this plot, we distinguish three dynamical stages: *MRI growth* ($t = 0$–$30 \times 10^3 \, M$), *relaxation* ($t = 30$–$75 \times 10^3 \, M$), and *steady state* ($t = 75$–$150 \times 10^3 \, M$).

Table 1
Properties of the Binary System for our Runs, and the Initial Values of l_{in} and Σ_0

	b [M]	$M^{(1,2)}$ [M]	Ω_{bin}	$a^{(1,2)}$	l_{in} [M]	Σ_0 [M^{-1}]
b20-spins	20	0.5	$b^{-3/2}$	$-0.9M^{(1,2)}$	8.62	0.1070
b20_v0	20	0.5	$b^{-3/2}$	0.0	8.60	0.1066
b20_v1	20	0.5	$b^{-3/2}$	0.0	8.60	0.1066
b20_v2	20	0.5	$b^{-3/2}$	0.0	8.60	0.1066
b20+spins	20	0.5	$b^{-3/2}$	$0.9M^{(1,2)}$	8.57	0.1063

Note. In every case the BHs separation is fixed to $b = 20M$, they have equal masses $M^{(1,2)} = 0.5M$, and move in Keplerian orbits with $\Omega_{bin} = b^{-3/2}$. We explore different values for the spins of the BHs. Notice runs b20_v0, b20_v1 and b20_v2 have identical settings. They only differ on the random initial perturbations on the internal energy u.

runs are identical and their only differences arise from stochastic processes triggered by random initial perturbations in the internal energy of the fluid. Specifically, given a physical quantity $\mathcal{P}_i$ with $i = 0, 1, 2$ for runs b20_v0, b20_v1, and b20_v2, we will express the result as $\langle \mathcal{P} \rangle_{a=0} \pm \sigma_{\mathcal{P}}$, where

$$\langle \mathcal{P} \rangle_{a=0} = \frac{1}{3} \sum_{i=0}^{2} \mathcal{P}_i \tag{43}$$

is the mean of $\mathcal{P}_i$ over the non-spinning runs, and

$$\sigma_{\mathcal{P}} = \sqrt{\sum_{i=0}^{2} \frac{(\langle \mathcal{P} \rangle_{a=0} - \mathcal{P}_i)^2}{3 - 1}} \tag{44}$$

is a coarse measure of the corresponding standard deviation. To determine whether a run with different parameters differs significantly from the three non-spinning runs, we measure the deviation Z of its prediction $\mathcal{P}'$, in units of standard deviations by

$$Z = \frac{\mathcal{P}' - \langle \mathcal{P} \rangle_{a=0}}{\sigma_{\mathcal{P}}}. \tag{45}$$

Following Noble et al. (2012), many of our results will be expressed in units of Σ_0, the initial maximum value of the surface density $\Sigma(r, \phi)$ (see Equation (A1)). These values are $\Sigma_0 = 0.1070M^{-1}$, $0.1066M^{-1}$, $0.1066M^{-1}$, $0.1066M^{-1}$ and $0.1063M^{-1}$ for runs b20-spins, b20_v0, b20_v1, b20_v2 and b20+spins, respectively (see Table 1).

5.1. Spin-Sensitive Results

The spin of a BH has important effects on matter orbiting near the horizon, but these effects decline rapidly with radius; frame-dragging terms in the effective gravitational potential for spinning black holes are $\propto r^{-3}$ (see Appendix B). For this reason, we do not expect the spin of the BHs will have a direct impact on the bulk properties of the circumbinary disk, whose inner edge lies at $r \approx 50M$. The accretion streams, on the contrary, reach distances close enough to the black hole that these effects may be relevant.

Since the accretion streams carry nearly all the matter accreted by the binary, we begin by exploring the effect of the spins on the accretion rate. For all three non-spinning cases, the time-averaged accretion rate at the inner boundary during the steady state period is (see Figure 3) $(5.0 \pm 0.4) \times 10^{-3} \sqrt{Mb} \, \Sigma_0$. Strikingly, runs b20-spins and b20+spins deviate from this mean value by $+5.7$ and -1.8 standard deviations, respectively. In other words, the circumbinary accretion rate is enhanced (reduced) by $+45\%$ (-14%) if the spin of the BHs are anti-parallel (parallel) to the angular momentum of the binary.

As found in previous works with similar parameters (Noble et al. 2012; Shi et al. 2012), a portion of the falling streams receives enough angular momentum from the binary and is flung back to the circumbinary disk, impacting the inner edge and causing strong shocks whose dissipation contributes significantly to the luminosity. Having found that the accretion rate is sensitive to spin, we might therefore expect that the luminosity is likewise. In particular, compared with non-spinning runs, the stronger streams of b20-spins should
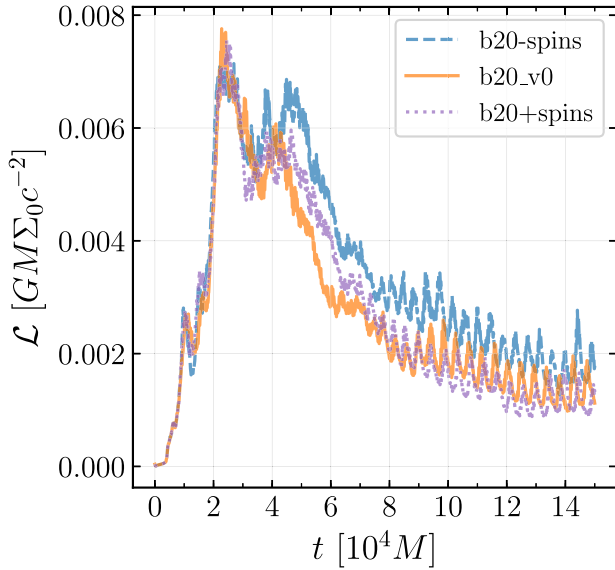
8

Figure 4. Integrated luminosity $\mathcal{L}$ (see Equation (A6)) as a function of time for three of our runs.

increase the total luminosity of the system, and the opposite for the weaker streams of b20+spins. In Figure 4 we plot $\mathcal{L}$ as a function of time for our runs. The average of $\mathcal{L}$ during the steady state period of non-spinning runs was $(1.76 \pm 0.07) \times 10^{-3} GM\Sigma_0 c^{-2}$. The corresponding averages for b20-spins and b20+spins depart from this mean by $+7.49$ and -3.17 standard deviations, respectively, a very significant effect. These differences correspond to a change of $+29\%$ and -12% in the total luminosity of the system, respectively, with respect to non-spinning runs.

Besides carrying the accretion flow and driving shocks that contribute to the integrated luminosity, the streams also play an important role in angular momentum transport. As they plunge toward the binary, the streams are subjected to strong torques by the binary. The portion of the stream flung back outward then transfers this added angular momentum to the inner edge of the circumbinary disk. As explained by Shi et al. (2012), because the local angular momentum $J = \int j^t \sqrt{-g}\, dV$ with $j^\mu = T^\mu{}_\phi$ should be constant in a time-steady disk, this supplemental angular momentum is transferred to adjacent layers by internal stresses.

To study the angular momentum budget of the circumbinary disk, we unpack $\partial_r \partial_t J$ into its several components. We refer the reader to Appendix C of Noble et al. (2012) for the explicit expansion (see also Farris et al. 2011). Five stresses contribute: the gravitational stress T_G, whose radial gradient produces the gravitational torque $T^\mu{}_\nu \Gamma^\nu{}_{\mu\phi}$; the Maxwell stress $\partial_r M^r{}_\phi$, which is the EM part of $T^r{}_\phi$; turbulent Reynold stresses $\partial_r R^r{}_\phi = \rho \delta u^r \delta u^\phi$, resulting from local perturbations of the fluid velocity; the advected Reynolds stress A^r_ϕ associated with the mean velocities u^r and u^ϕ; and the radiative stress $\mathcal{F}_\phi$ from the radiative cooling function. Summed, these produce the local torque

$$\partial_r \partial_t J = \partial_r T_G - \{\mathcal{F}_\phi\} - \partial_r \{M^r{}_\phi\}$$
$$- \partial_r \{R^r{}_\phi\} - \partial_r \{A^r{}_\phi\}. \qquad (46)$$

In Figure 5 we plot each term on the rhs of Equation (46) as a function of r, averaged over the period $t = 70$–$150 \times 10^3\, M$. The total angular momentum flux (black) is approximately

constant as a function of radius, as expected for a steady state flow. In the cavity (i.e., $r < 2b$), there is a significant difference between our non-spinning and spinning runs. The maximum of the gravitational torque (blue) for non-spinning runs is $(2.011 \pm 0.053) \times 10^{-2} Mb\Sigma_0$, while b20-spins and b20+spins differ by 7.11 and -2.40 standard deviations, respectively. In other words, the stronger (weaker) streams from b20-spins (b20+spins) increase (reduce) the maximum of the gravitational torque density by 18% (-6%). The Reynold stresses (green) are increased (reduced) accordingly because once additional angular momentum is deposited by gravitational torques, it must be carried away by fluid motions.

Contrasts in accretion rate must also, through mass conservation, affect the radial distribution of mass in the system. To search for this effect, we contrast the surface density of gas $\Sigma(r, \phi)$ (see Equation (A1)) in the corotating frame of the binary with the surface density in non-spinning runs:

$$\eta_\Sigma(r, \phi_{\rm cor}) = \frac{\Sigma(r, \phi_{\rm cor})[\Sigma_0] - \langle \Sigma(r, \phi_{\rm cor})[\Sigma_0] \rangle_{a=0}}{\langle \Sigma(r, \phi_{\rm cor})[\Sigma_0] \rangle_{a=0}}, \qquad (47)$$

where $\phi_{\rm cor} = \phi - \Omega_{\rm bin} t$, and the brackets $[\Sigma_0]$ denote that each surface density is taken in units of their initial maximum Σ_0. In Figure 6 we plot the average of this residual over the steady state period for b20-spins (left) and b20+spins (right), and in Figure 7 we plot the averaged surface density in the corotating frame of the binary for non-spinning runs, which is the reference function for the latter residuals.

The residual $\eta_\Sigma(r, \phi_{\rm cor})$ is greatest inside the cavity, where the spin effects should be largest. The sign of the effect is such that the residual in the cavity is positive for b20-spins but negative for b20+spins—and flips in the bulk of the circumbinary disk ($r > 4b$). This is consistent with our results on enhanced (reduced) circumbinary accretion. If, independent of spin, the system is in approximate inflow equilibrium, enhancement (or reduction) of the accretion rate implies that, averaged over time, the cavity must contain more (or less) gas mass for a fixed mass near the circumbinary disk's inner edge. In addition, the outer disk is drained a bit more when there is a higher accretion rate at its inner edge when all the different initial disk masses were the same.

Beyond the amount of matter and angular momentum that the streams carry, the spin of the BHs may affect the streams' trajectories. In Figure 8 (top) we plot the averaged surface density during the steady state period, in the corotating frame of the binary, evaluated at the radial inner boundary of the domain $r_{\rm in}$, for spinning runs and the average of non-spinning runs (b20_av). We notice two distinctive peaks at $\phi_{\rm cor} \approx 0.06\pi, 1.06\pi$ that we associate with the narrow streams that fall toward each BH (see also Figure 7). At a first glance, the curves for spinning and non-spinning runs look equivalent, but the zoom-in plot, and the percent deviations (bottom), show some interesting results. First, we notice the peaks for the different runs are shifted in $\phi_{\rm cor}$, in ascending order b20-spins, b20_av, b20+spins. Regarding the percent deviations of spinning runs, we notice b20-spins finds local maxima behind the peaks of the surface density, and local minima ahead, and b20+spins present the opposite behavior. In the next subsection, we explain these results from the effective gravitational potential of spinning binaries.
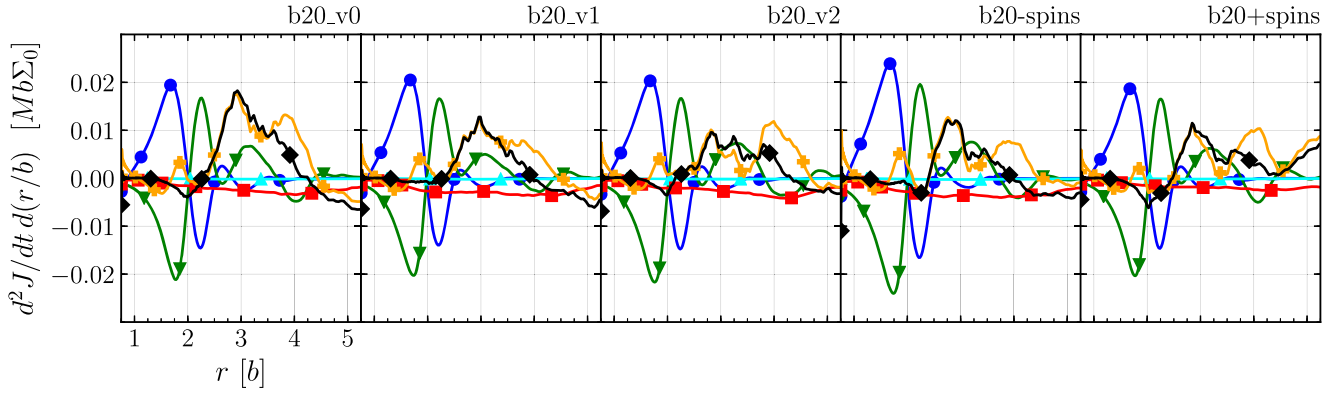
Figure 5. Shell-integrated torques as a function of r, averaged over the period $t = 70–150 \times 10^3$ M. We distinguish the gravitational torques exerted by the binary (blue/circle), Maxwell stresses (red/square), Reynolds or turbulent torques (green/down triangle), the density of advected angular momentum (gold/plus), radiative losses (cyan/triangle up), and the net flux of angular momentum (black/diamond).
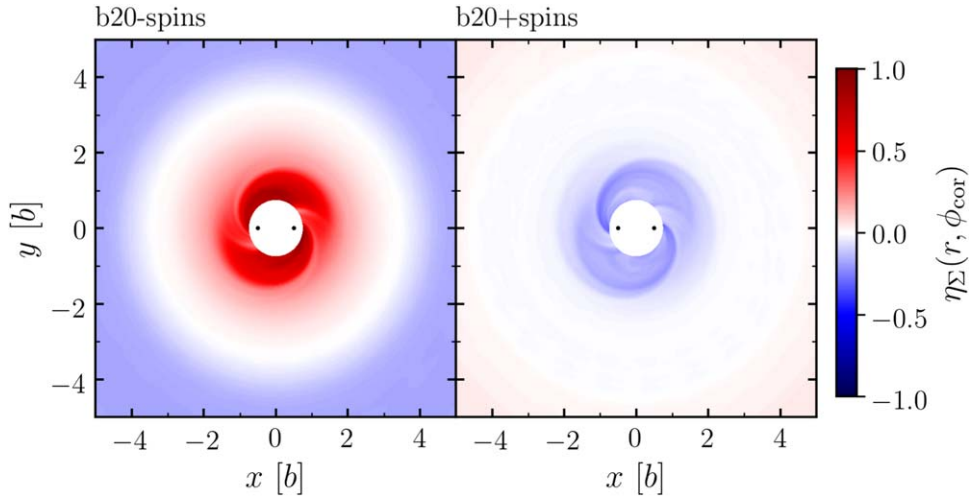

Figure 6. Residuals of the surface density with respect to non-spinning runs for `b20-spins` (left) and `b20+spins` (right), averaged over the steady state period (see Equation (47)).
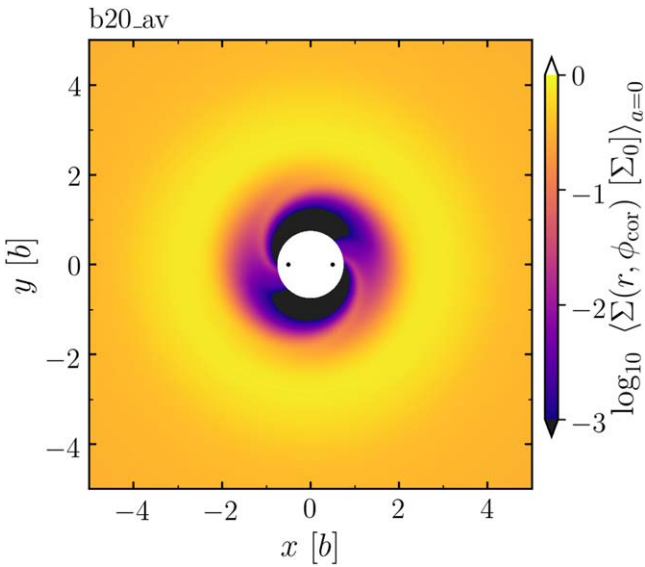
Figure 7. Average of the surface density over the steady state period for non-spinning runs, in the corotating frame of the binary (logarithmic scale). We notice the piling-up of matter in the inner region $2b < r < 4b$, the evacuated inner cavity in $r < 2b$, and the falling streams toward each BH. This function is the reference for the residuals in Figure 6.
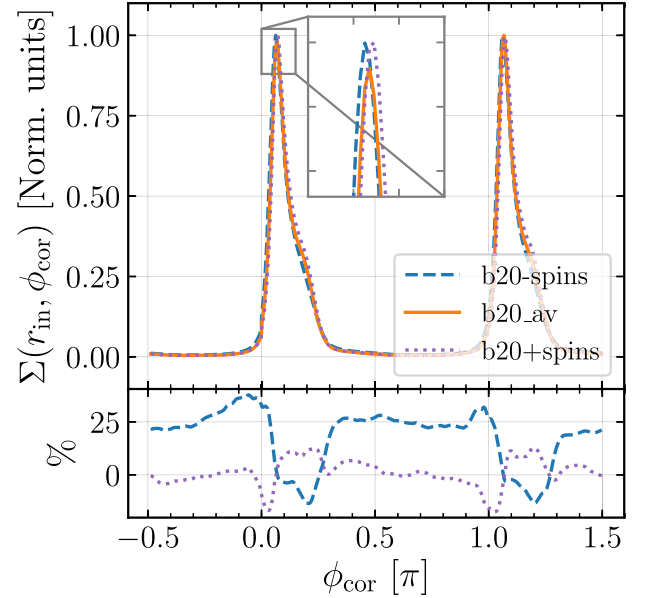
Figure 8. Top: surface density, averaged during the steady state period, in the corotating frame of the binary, and evaluated at the radial inner boundary of the domain r_{in}, for spinning runs and the average of non-spinning runs (`b20_av`). Bottom: percent deviation of curves for spinning runs with respect to the non-spinning average.

5.2. Interpretation of Spin-sensitive Results

In Section 5.1 we found that the spin of the BHs in a binary system has significant effects on the circumbinary accretion and related quantities. In this subsection, we explain the causes of these effects in simple physical terms.

In Appendix B, we analyze the EoM of particles orbiting near spinning binaries. We find the spin of the BHs introduces two effects to the lowest PN expansion of the gravitational potential. First, the spin couples to the orbital velocity of the BH, as seen from the second and fourth terms of Equation (B8). Far from the source and averaging in ϕ, however, this effect is canceled for the case of identical BHs. The second effect is frame-dragging, or twist of spacetime geodesics, as seen in Equation (B15). Interestingly, this effect remains after expanding for large radius r and averaging in ϕ, and couples to the orbital angular momentum of the fluid. In the following, we explore how this term affects the process of stream formation and accretion.

Shi & Krolik (2015) found that, in the phase-space of positions and velocities of the orbiting fluid, the volume of infalling trajectories from the inner edge of the circumbinary disk is severely constrained. Gas with angular momentum close to the circular orbit angular momentum at the inner-edge radius falls in so slowly that the binary torques raise its angular momentum and the gas is cast back out to the circumbinary disk. Only gas with angular momentum at least $\simeq 15\%$ less than that of a circular orbit can fall in quickly enough to avoid acquiring too much angular momentum. Such gas parcels must, in addition, begin their fall from a specific angle relative to the binary separation axis. The upper limit for the angular momentum J of the fluid to be accreted is well approximated by the condition $\Phi_{\rm eff}(r_{\rm in}) \leqslant 0$, where $\Phi_{\rm eff}$ is the gravitational effective potential of the binary, evaluated at the inner boundary of the domain. As derived in Equation (B15):

$$\Phi_{\rm Eff} = -\frac{M}{r} - \frac{1}{16}\frac{b^2 M}{r^3} + \frac{J^2}{2r^2} + \frac{MJ}{3r^3}\left(2a + \frac{L}{4}\right). \quad (48)$$

The condition $\Phi_{\rm eff}(r_{\rm in}) \leqslant 0$ is equivalent to $J \leqslant (6.54, 6.51, 6.48)$ for $a = (-0.9, 0, 0.9)$, respectively. In other words, spins opposite (parallel) to the angular momentum of the binary extend (reduce) the volume of infalling trajectories in the phase-space of position and velocity of the orbiting fluid. This fact explains the enhanced (reduced) accretion in the run b20-spins (b20+spins).

In Figure 8 we noticed the accretion streams for b20-spins (b20+spins) lie behind (ahead) in $\phi_{\rm cor}$ with respect to non-spinning runs. In other words, the gas swings in azimuth by a smaller (larger) angle while traversing the cavity before passing through the inner boundary. This is also consistent with frame-dragging effects.

5.3. Spin-insensitive Results and Comparison with Previous Works

In this subsection, we describe the properties of the circumbinary disk that are not significantly affected by spins, but the length of our simulations has revealed new aspects of them, not seen in previous, shorter simulations.

In binaries with mass-ratio close to unity and low orbital eccentricity, a remarkable $m = 1$ mode in the ϕ-distribution of matter develops in the radial range $2b < r < 4b$; the so-called *lump*. This lump arises as a result of phase-coherence in the
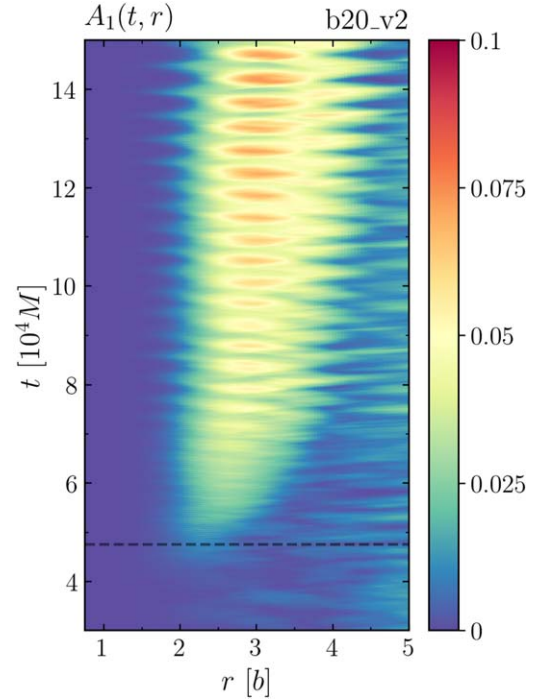

Figure 9. Power of $m = 1$ mode of the vertically integrated density, as function of radii and time, for b20_v2. We notice the growth and saturation of the lump at $2b < r < 4b$. The dashed line represents the moment of lump formation $t_{\rm lump}$.

trajectory of matter that falls a short way but then is propelled back out after the binary torques add to its angular momentum (see Noble et al. 2012; Shi et al. 2012; D'Orazio et al. 2013; Farris et al. 2014; Miranda et al. 2016; Tang et al. 2017). As we will show, our longer simulations reveal that the dynamics of the lump are predictable from the time of its formation, and its orbit stabilizes after $\Delta t \sim 40 \times 10^3\,M$.

To characterize the amplitude of the lump, we calculate the power of the Fourier modes $m = 0$ and $m = 1$ in the vertically integrated density as a function of radius and time (see Equation (A8), and Cuadra et al. 2009; Noble et al. 2021). We denote these modes $A_0(t, r)$ and $A_1(t, r)$, respectively. In Figure 9, we plot $A_1(t, r)$ for b20_v2 and, indeed, we notice the growth and saturation of the lump at $2b < r < 4b$.

To determine the time $t_{\rm lump}$ when the lump forms, we integrate $A_m(t, r)$ over the radial range $2b < r < 3b$ and define $t_{\rm lump}$ as the time when the ratio of this integral of $A_1(t, r)$ to the total surface density (this integral of $A_0(t, r)$) is larger than 0.2. To visualize the different $t_{\rm lump}$ for each run, in Figure 10 we plot the evolution of the ratio of the $m = 1$ and $m = 0$ integrals for our runs. For non-spinning runs, the lump forms at 36390, 64650, 47550 M, resulting in an average $t_{\rm lump} = (5.0 \pm 1.5) \times 10^4\,M$. In Figure 11 (top, right) we plot the surface density $\Sigma(r, \phi)$ (see Equation (A1)) at $t = t_{\rm lump}$ for b20_v0, where we notice the recently formed lump in the positive y hemisphere. For runs b20-spins and b20+spins, the lump forms at 50280M and 39690M, respectively, in concordance with non-spinning values.

To characterize the orbital dynamics of the lump, we define $r_{\rm lump}(t)$ as the radial position of the maximum value of $A_1(t, r)$ as a function of time (see Figure 9). We define $\Omega_{\rm lump}(t)$ in terms of the time-derivative of the Fourier phase for the $m = 1$ mode (see Equation (A11), and Noble et al. 2021). Lastly, we define the eccentricity $e_{\rm lump}(t)$ in terms of the ratio between the lump's
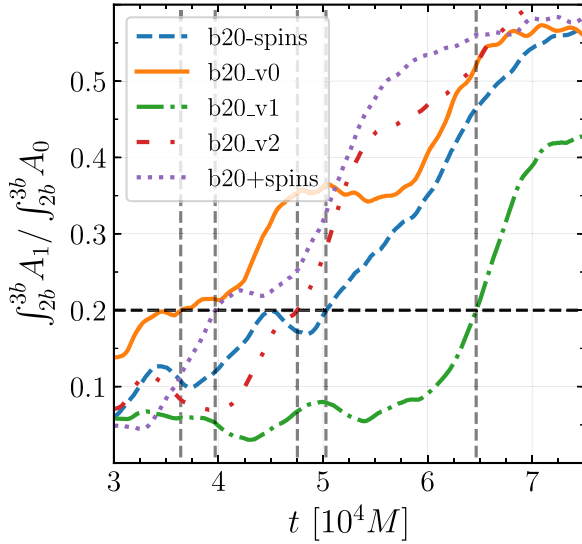
Figure 10. Evolution of the ratio of the power of the Fourier mode $m = 1$ and $m = 0$ of the vertically integrated surface at the lump formation region. The intersection of the black dashed and gray dashed defines the time of lump formation. In ascending order, $t_{\text{lump}}/M = 36390, 39690, 47550, 50280, 64650$.
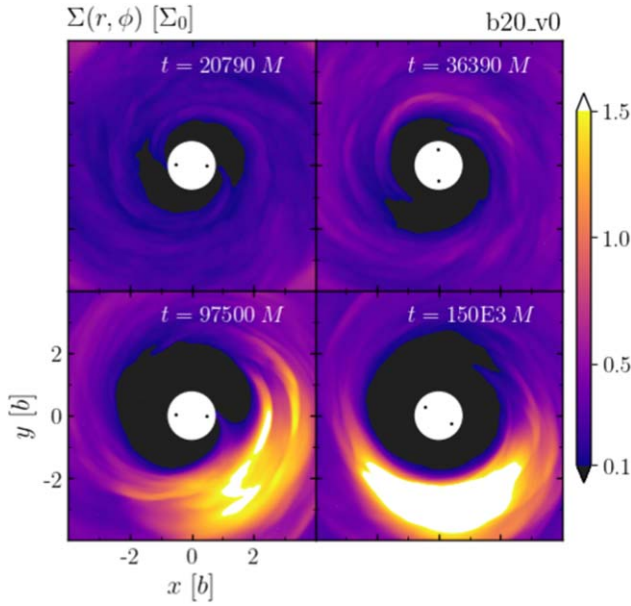

Figure 11. Surface density $\Sigma(r, \phi)$ in units of Σ_0 at different times for run b20_v0. We distinguish the double accretion streams during the first orbits of the binary (top, left), the formation of the lump (top, right), the growth of the lump and the transition to a single accretion stream (bottom, left), and the saturated lump at the end of the simulation (bottom, right).

radial and azimuthal velocity components (see Equation (A5) and Shi et al. 2012). In Figure 12 we plot these quantities as a function of $t - t_{\text{lump}}$, for each of our runs. In each of the three panels, the curves follow very nearly the same paths. This means that, although t_{lump} is subject to a considerable dispersion among our runs, once the lump forms, its dynamics are robust and predictable.

In Figure 12 we notice the orbit of the lump stabilizes after $\Delta t \sim 40 \times 10^3 \, M$. Its radial position r_{lump} grows approximately linear in time and then gradually equilibrates. For the first $\Delta t = 20 \times 10^3 \, M$, non-spinning runs present $r_{\text{lump}} = (2.48 \pm 0.05) \, b$, but for the last $\Delta t = 4 \times 10^{t} 3 \, M$ we find
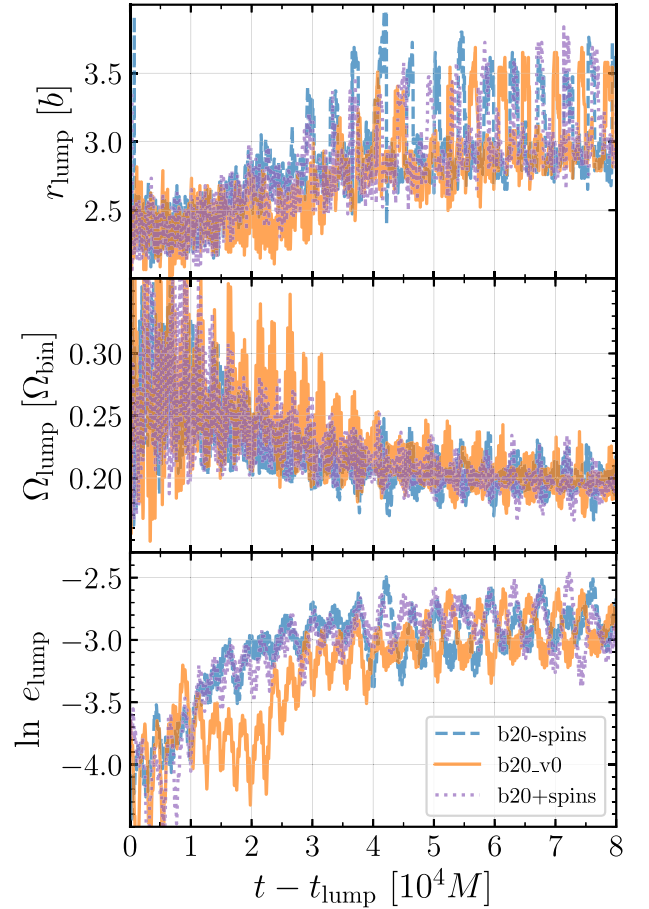
Figure 12. Evolution of the radial position of the lump (top), its orbital frequency (middle), and orbital eccentricity (bottom). We plot the evolution of these quantities from the moment of lump formation t_{lump} until $t_{\text{lump}} + 8 \times 10^4 \, M$.

$r_{\text{lump}} = (3.05 \pm 0.05) \, b$. The angular frequency of the lump decreases accordingly, following a Keplerian behavior. For the first $\Delta t = 20 \times 10^3 \, M$ we find $\Omega_{\text{lump}} = (0.25 \pm 0.01) \, \Omega_{\text{bin}}$ but for the last $\Delta t = 40 \times 10^3 \, M$ it reduces to $\Omega_{\text{lump}} = (0.197 \pm 0.003) \, \Omega_{\text{bin}}$. This values are in agreement with previous works. While the early value of Ω_{lump} agrees with Noble et al. (2012) who evolved the system for the earlier stages of the lump development, the stabilized value of Ω_{lump} agrees with longer two-dimensional hydrodynamical simulations (e.g., Miranda et al. 2016). Regarding the eccentricity, initially we find $\ln e_{\text{lump}} = -3.6 \pm 0.2$ for non-spinning runs, but later it stabilizes to $\ln e_{\text{lump}} = -2.91 \pm 0.04$, in agreement with results from Shi et al. (2012). Regarding our spinning runs, every quantity lies within ± 1.5 times the standard deviation, implying the dynamics of the lump are independent of the spin of the BHs.

In addition to the overdense lump, matter tends to pile up at the inner edge of the circumbinary disk. This is as a consequence of the interplay between the internal stresses that remove angular momentum from matter just outside the inner edge and the gravitational torques that add angular momentum to streams in the cavity inside the inner edge. Our longer simulations reveal that this *piling-up* saturates during the steady state. To analyze the dynamics of this overdense region, in Figure 13 we plot the θ-integrated and ϕ-averaged density $\Sigma(r)$ (Equation (A2)) in the period $t = 70–150 \times 10^3 \, M$. Each curve represents an average over $\Delta t = 2 \times 10^3 \, M$ and, through colors
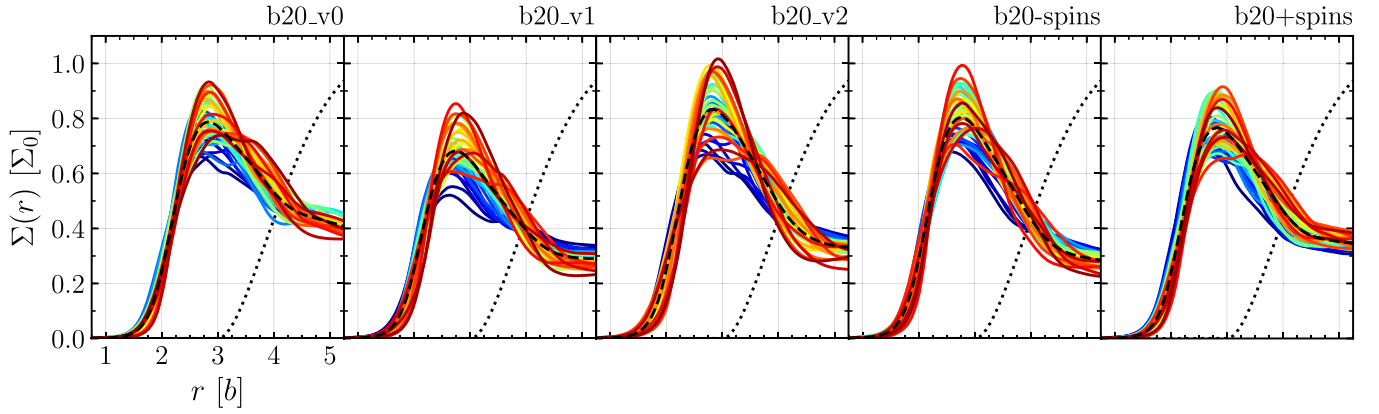
Figure 13. Vertically integrated and ϕ-averaged density $\Sigma(r)$ averaged over $\Delta t = 2 \times 10^3\, M$ for the period $t = 70\text{–}150 \times 10^3\, M$ (violet to red curves). The dotted curve represents the initial data, and the dashed curve the average of colored curves.
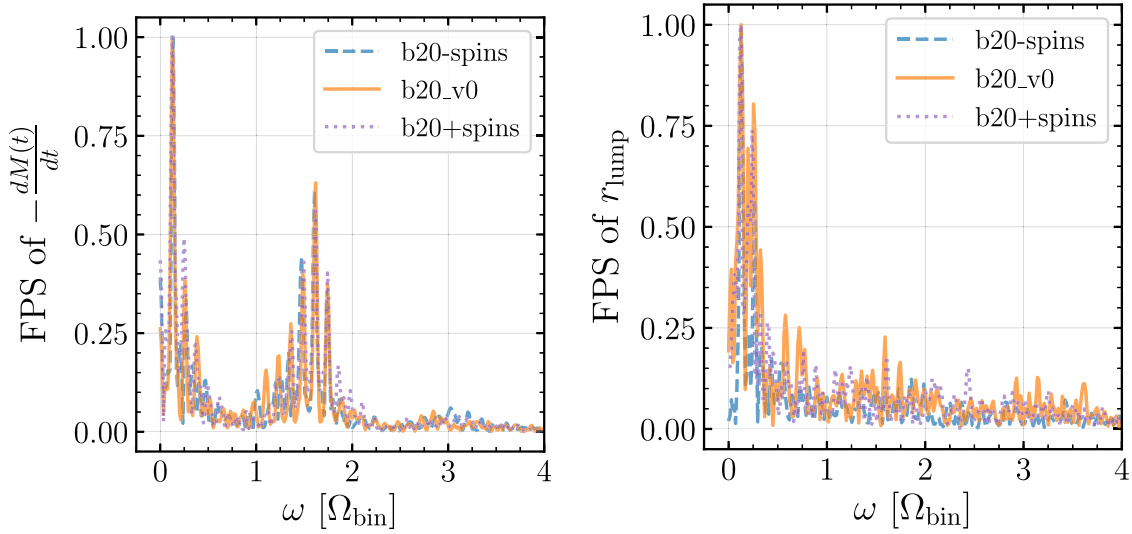

Figure 14. Fourier power spectrum of the accretion rate at the innermost radial boundary of the domain during the steady state period (left), and of the radial position of the lump in the interval $40 \times 10^3\, M < t - t_{\text{lump}} < 80 \times 10^3\, M$ (right). To enhance the periodic behavior, we analyze the difference of these quantities with adjusted polynomials of first order, and we apply a Blackman–Harris window function.

violet to red, they span the entire steady state period. The maximum of the averaged curves (dashed) for non-spinning runs is $(0.76 \pm 0.07)\,\Sigma_0$, and its radial position is $(2.80 \pm 0.06)\,b$. Noble et al. (2012) found that, when the binary evolution is frozen, the peak surface density increased steadily up to $t \approx 75 \times 10^3\, M$; Figure 13 reveals that their simulation stopped just at the point where the growth in peak surface density ceases.

The length of our simulations makes them ideal to study the characteristic frequencies of the system. As expected from the predominant quadrupole mode of the binary potential, accretion into the inner boundary is initially carried by two narrow streams that extend from the inner edge of the disks toward each BH (see Figure 11 (top, left)). In the steady state, however, accretion is dominated by a single stream that is produced when a BH passes near the lump (see Figure 11 (bottom, left)). The frequency of this occurrence is $2(\Omega_{\text{bin}} - \Omega_{\text{lump}}) \sim 1.6\Omega_{\text{bin}}$. Indeed, in Figure 14 (left) we plot the Fourier Power Spectrum (FPS) of the accretion rate during the steady state (see also Figure 3) and find the expected peak at $\omega = 1.6\Omega_{\text{bin}}$. Figure 14 (left) also presents a strong peak at $\omega = 0.12\Omega_{\text{bin}}$, which corresponds to a lower-frequency

modulation of the accretion rate, as seen in the spikes of Figure 3 during the steady state.

This modulation is caused by an oscillation of the radial position of the lump. Indeed, in Figure 14 (right) we plot the FPS of $r_{\text{lump}}(t)$ during the stabilized period of the orbit of the lump $40 \times 10^3\, M < t - t_{\text{lump}} < 80 \times 10^3\, M$ (see also Figure (12) (top)), and find its maximum at $\omega = 0.12\Omega_{\text{bin}}$. The causes of this radial oscillation will be addressed in subsequent work.

Although the bimodal distribution of the FPS of the accretion rate at the cavity is in agreement with previous works (MacFadyen & Milosavljević 2008; Shi et al. 2012; D'Orazio et al. 2013; Muñoz and Lai 2016, among others), the precise values of the peak frequencies claimed in this work differ with such references.

In the following, we analyze if our longer simulations approach inflow equilibrium. In Figure 15 we plot the average of the radial profile of the accretion rate (see Equation (A4)) over the period $t = 70\text{–}150 \times 10^3\, M$ (dashed, red), and over four equally spaced sub-periods with $\Delta t = 20 \times 10^3\, M$ (*dark* to *light* curves). While we notice the average curve has a systematic growth from $r > 3b$, implying the disk has not reached inflow equilibrium, we also notice an improvement of this inflow condition if compared with previous three-
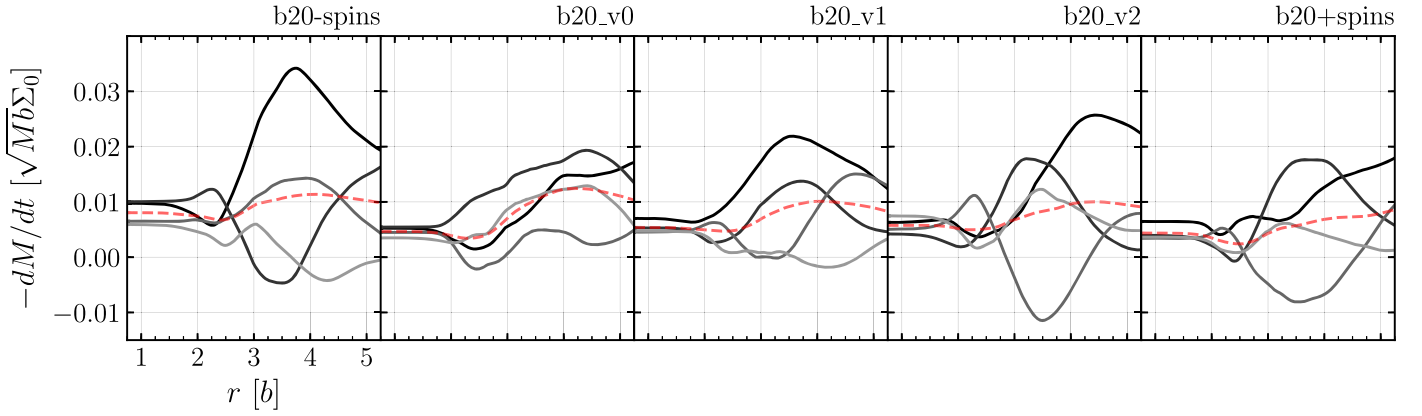
Figure 15. Top: accretion rate as a function of r averaged over $\Delta t = 20 \times 10^3 M$ in the period $t = 70$–$150 \times 10^3\,M$ (dark to light curves), and the average over the full period (dashed, red).

dimensional MHD simulations that evolved the system for earlier stages (Noble et al. 2012; Shi et al. 2012). In those earlier papers, the ratio of the accretion rate at $r \simeq 3 - 4b$ to the accretion rate crossing the inner edge was about a factor of 3; extending the duration of the simulation from $70 \times 10^3\,M$ to $150 \times 10^3\,M$ reduces that contrast to a factor ≈ 1.5. Thus, for these conditions, the inflow equilibration time at this radius is $t \sim 10^5\,M$.

Interestingly, also in Figure 15, we notice periods when the accretion rate becomes negative at regions close to the inner edge of the disk.

Finally, we analyze the mechanisms of angular momentum transport during the steady state of our longer runs. Comparing our results on shell-integrated torques in Figure 5 with those of Shi et al. (2012) and Noble et al. (2012) for earlier epochs of the system, we find that during the steady stage Maxwell stresses (red) are significantly reduced at the bulk of the disk. On the contrary, Reynolds stresses are strengthened and show traces of a propagating wave through the fluid. Shi & Krolik (2015) also found a significant growth of turbulent torques in the steady state period of a related system, and associated it with the propagation of a single-armed wave. We will study these issues in detail in a subsequent work.

5.4. Summary

We found the spin of the BHs have a direct impact on processes that take place in the inner cavity. Specifically, negative (positive) spins enhance (reduce) the circumbinary accretion by $+45\%$ (-14%) with respect to the non-spinning case. The stronger (weaker) accretion streams enhance (decrease) the globally integrated luminosity by $+29\%$ (-12%), and the peak of the gravitational torques at the cavity by $+18\%$ (-6%), with respect to non-spinning runs. In the long-term, these effects can discreetly influence the bulk of the disk, as we found a reduction (increment) of the surface density for $r > 4b$. Finally, we found that the spin of the BH affects the shape of the accretion streams, as they fall behind (advanced) in ϕ with respect to the non-spinning case. Other properties of the circumbinary such as the dynamics of the lump, the piling-up of matter at the inner edge, or the radial profile of the accretion rate, remain unaffected by the spin of the BHs.

The length of our runs allowed us to reach an unprecedented steady state in three-dimensional GRMHD simulations. We found interesting differences with respect to early epochs, as described by Shi et al. (2012) and Noble et al. (2012). In

particular, the dynamics of the lump are robust and predictable since its formation and its orbit stabilizes after $\Delta t \sim 40 \times 10^3\,M$, the growth of the lump and the piling up of matter at the inner edge of the disk saturates and remains steady, there are regions within the inner part of the circumbinary where the accretion rate becomes negative, and the role of Reynolds stresses grow at the bulk of the disk, but the role of Maxwell stresses diminishes, revealing a demagnetization of the plasma. We intend to explore these results in detail in an upcoming work.

6. Conclusions

We presented a new approximate metric for the spacetime of widely separated BBHs in the relativistic regime ($b \geqslant 20M$). This metric is unique in the sense that it can be used in the strong field regime, is easy to implement, it has an optimal performance, and includes the spins of the BHs as free parameters. We computed and analyzed its Ricci scalar R at different scales and concluded the metric is an acceptable approximation for a vacuum solution of EFE. Further, we proved its expansion agrees with the lowest PN expansion of the metric of a binary system of spinning BHs.

As a first application, we set and evolved a series of magnetized circumbinary disks around an equal-mass binary system, with separation fixed at $b = 20M$. We explored different values for the spins of the BHs, aligned and counter-aligned with the orbital angular momentum of the binary, and performed three identical non-spinning runs to study the effect of random perturbations in our predictions (see Table 1). We followed closely the techniques of Noble et al. (2012) that explored the same system (non-spinning) but for earlier stages and with a different approach and gauge for the spacetime construction. We evolved the system for longer than previous three-dimensional MHD simulations, until $t = 150 \times 10^3\,M$ or 266 orbits of the binary system. We noticed that the circumbinary disk reaches a steady state from $t = 75 \times 10^3\,M$ onwards, and focused our results on this period. Our results are consistent with previous works on non-spinning binaries, and with expectations for the effect of the spins on the circumbinary disks, proving the physical validity of the SKS spacetime. We conclude the spin of the BHs, via frame-dragging effects, can significantly affect the circumbinary accretion and luminosity. Specifically, spins counter-aligned (aligned) with the orbital angular momentum of the binary enhance (reduce) the circumbinary accretion with respect to the

non-spinning case. Further, the spin twists the spacetime geodesics at the cavity, and the streams reach the inner cavity behind (forward) in ϕ with respect to the non-spinning case. We will explore the dynamics of mini-disks around spinning binaries in a subsequent work (Combi et al. 2021).

Appendix A
Diagnostics

We summarize usual conventions and quantities used in the analysis of accretion disks:

1. Surface density:

$$\Sigma(r, \phi) = \frac{\int \rho \sqrt{-g} \, d\theta}{\sqrt{g_{\phi\phi}(\theta = \pi/2)}}, \tag{A1}$$

and its ϕ-average:

$$\Sigma(r) = \frac{\int \rho \sqrt{-g} \, d\theta \, d\phi}{\int \sqrt{g_{\phi\phi}(\theta = \pi/2)} \, d\phi}. \tag{A2}$$

2. Height of the disk:

$$H = \frac{\langle \rho \sqrt{g_{\theta\theta}} | \theta - \pi/2 | \rangle}{\langle \rho \rangle}. \tag{A3}$$

3. Accretion rate as a function of r:

$$\frac{dM(r)}{dt} = -\int \rho u^r \sqrt{-g} \, d\theta \, d\phi. \tag{A4}$$

4. Eccentricity of the fluid in the lump region:

$$e_{\text{lump}} = \frac{\left| \int_{2b}^{4b} \langle h v_r e^{i\phi} \rangle \, dr \right|}{\int_{2b}^{4b} \langle h v_\phi \rangle \, dr}. \tag{A5}$$

5. Integrated luminosity:

$$\mathcal{L} = \int u_t \mathcal{L}_c \sqrt{-g} \, dr \, d\theta \, d\phi. \tag{A6}$$

6. Fourier transformation with respect to ϕ of the vertically integrated density:

$$\mathcal{B}_m(r, t) = \{\rho e^{im\phi}\}, \tag{A7}$$

and the corresponding mode power

$$A_m(r, t) = |\mathcal{B}_m(r, t)|. \tag{A8}$$

7. Since the vertically integrated surface is a real function, its Fourier modes satisfy:

$$\mathcal{B}_m(r, t) e^{im\phi} = \text{Re} [\mathcal{B}_m(r, t)] \cos(\phi) - \text{Im} [\mathcal{B}_m(r, t)] \sin(\phi). \tag{A9}$$

The maximum of these modes is found at the phase:

$$\phi_m(r, t) = \arctan \left[-\frac{\text{Im} [\mathcal{B}_m(r, t)]}{\text{Re} [\mathcal{B}_m(r, t)]} \right]. \tag{A10}$$

where the function arctan is defined to return the value of ϕ_m in the range $[0, 2\pi]$, checking on the sings of $\text{Im} [\mathcal{B}_m(r, t)]$ and $\text{Re} [\mathcal{B}_m(r, t)]$. Identifying the phase of the lump as the maximum of the $m = 1$ mode integrated at the lump region $2b < r < 4b$, we obtain the angular frequency of the lump:

$$\Omega_{\text{lump}} = \frac{d}{dt} \phi_{m=1}(t). \tag{A11}$$

Appendix B
Post-Newtonian Approximation

The linearity of the SKS metric (11) implies that its expansion to the lowest order in the boost velocities and large radius, reproduces the lowest PN metric of a spinning compact binaries (see Tagoshi et al. 2001):

$$g_{00} = -(1 + 2\Phi) + \mathcal{O}(v_K^2), \tag{B1}$$

$$g_{ij} = \delta_{ij}(1 - 2\Phi) + \mathcal{O}(v_K^2), \tag{B2}$$

$$g_{0i} = -4\xi_i + \mathcal{O}(v_K^2), \tag{B3}$$

where the scalar and vector potentials read:

$$\Phi := -\frac{M^{(1)}}{r^{(1)}} - 2\frac{S^{(1)ij} \tilde{r}^{(1)i} v_K^{(1)j}}{r^{(1)2}} + [(1) \to (2)], \tag{B4}$$

$$\xi_i := \frac{M^{(1)}}{r^{(1)}}v^{(1)i} + 2\frac{\check{r}^{(1)k}}{r^{(1)2}}S^{(1)ki} + [(1) \rightarrow (2)], \qquad (B5)$$

being $S^{(n)ij} := \epsilon^{ijk}S^{(n)k}$ with $S^{(n)k} := \delta_z^k M^{(n)}a^{(n)}$ for spins aligned with the z-axis, $r^{(n)} = (x^{(n)}, y^{(n)}, z^{(n)})$ the positional vector referred to the nth BH frame, $\check{r}^{(n)i} = r^{(n)i}/r^{(n)}$, and $v_K^{(n)i}$ the spatial velocity of the nth BH.

In the PN approximation, the EoM for a test particle with velocity $\boldsymbol{V}$ are given by the so-called gravitomagnetic analog of Lorentz equations (see, for instance, Mashhoon 2003):

$$\frac{dV^i}{dt} = -\nabla^i\Phi - (\boldsymbol{V} \times (\nabla \times \boldsymbol{\xi}))^i. \qquad (B6)$$

In the following we derive the dominant terms in these equations for the case of identical BHs orbiting in circular orbits, and we discuss the effect of the spins.

The scalar potential can be written as:

$$\Phi = -\frac{M^{(1)}}{r^{(1)}} + 2\frac{\check{r}^{(1)} \cdot (\boldsymbol{S}^{(1)} \times \boldsymbol{v}_K^{(1)})}{r^{(1)2}} + [(1) \rightarrow (2)] \qquad (B7)$$

$$= -\frac{M^{(1)}}{r^{(1)}} + 2\frac{M^{(1)}a^{(1)}v_K^{(1)}\cos\phi^{(1)}}{r^{(1)2}} + [(1) \rightarrow (2)], \qquad (B8)$$

where $\boldsymbol{S}^{(n)} \times \boldsymbol{v}_K^{(n)}$ points toward the center of mass and thus $\phi^{(n)}$ is the angle between $\check{r}^{(n)}$ and $-\check{r}_K^{(n)}$, being $\check{r}_K^{(n)} = \boldsymbol{r}_K^{(n)}/|\boldsymbol{r}_K^{(n)}|$ the normalized vector of the position of the nth BH (see Equations (15) and (16)). The second and fourth terms in Equation (B8) represent spin–orbit coupling effects.

Taking into account the following expressions:

$$r^{(1,2)2} = r^2 + \frac{1}{4}b^2 \mp rb\cos(\phi - \Omega_{\text{bin}}t), \qquad (B9)$$

$$\cos\phi^{(1,2)} = \frac{\pm x_K^{(1,2)} \mp x}{r^{(1,2)}}, \qquad (B10)$$

where b is the separation of the binary, $\boldsymbol{r} = (x, y, z)$ is the position vector of the particle in Cartesian coordinates with respect to the center of mass of the binary, and $\phi = \arctan(y/x)$, we expand Equation (B8) for large radius r and average in ϕ and t, to obtain:

$$\Phi = -\frac{M}{r} - \frac{1}{16}\frac{b^2M}{r^3} + \mathcal{O}\left(\frac{1}{r^4}\right), \qquad (B11)$$

where $M = M^{(1)} + M^{(2)}$. In this equation we recognize the well-known multipole expansion of equal-mass binaries in the Newtonian regime (see, for instance, MacFadyen & Milosavljević 2008). We also notice that spin–orbit coupling terms canceled out in this limit, because of the symmetries of the system.

Regarding the vector potential ξ_i, we obtain the Cartesian components:

$$\boldsymbol{\xi} = \frac{M^{(1)}}{r^{(1)}}\boldsymbol{v}^{(1)} + 2\frac{a^{(1)}M^{(1)}}{r^{(1)3}}$$
$$\times (y^{(1)}, -x^{(1)}, 0) + [(1) \rightarrow (2)]. \qquad (B12)$$

Replacing this expression in the second term of Equation (B6), transforming to a spherical basis, expanding for large radius r,

and averaging in ϕ, we obtain the radial component:

$$(\boldsymbol{V} \times (\nabla \times \boldsymbol{\xi}))^r = \frac{MJ}{r^4}\left(2a + \frac{L}{4}\right) + \mathcal{O}\left(\frac{1}{r^5}\right), \qquad (B13)$$

where we have defined $J = xV^y - yV^x$ as the specific angular momentum of the particle, $L = bv_K^{(1)} = bv_K^{(2)}$ as the specific orbital angular momentum of the binary, and $a = a^{(1)} = a^{(2)}$.

Applying Newton's second law in spherical coordinates for the force terms derived from Equations (B11) and (B13), we obtain:

$$\ddot{r} = -\frac{M}{r^2} - \frac{3}{16}\frac{b^2M}{r^4} + \frac{J^2}{r^3}$$
$$+ \frac{MJ}{r^4}\left(2a + \frac{L}{4}\right) + \mathcal{O}\left(\frac{1}{r^5}\right). \qquad (B14)$$

The latter equation of motion can be derived from the effective potential:

$$\Phi_{\text{Eff}} = -\frac{M}{r} - \frac{1}{16}\frac{b^2M}{r^3} + \frac{J^2}{2r^2}$$
$$+ \frac{MJ}{3r^3}\left(2a + \frac{L}{4}\right) + \mathcal{O}\left(\frac{1}{r^4}\right). \qquad (B15)$$

ORCID iDs

Federico G. Lopez Armengol ⓘ https://orcid.org/0000-0002-4882-5672
Luciano Combi ⓘ https://orcid.org/0000-0002-5427-1207
Manuela Campanelli ⓘ https://orcid.org/0000-0002-8659-6591
Scott C. Noble ⓘ https://orcid.org/0000-0003-3547-8306
Julian H. Krolik ⓘ https://orcid.org/0000-0002-2995-7717
Dennis B. Bowen ⓘ https://orcid.org/0000-0002-7447-1142
Mark J. Avara ⓘ https://orcid.org/0000-0001-9562-9677
Vassilios Mewes ⓘ https://orcid.org/0000-0001-5869-8542
Hiroyuki Nakano ⓘ https://orcid.org/0000-0001-7665-0796

References

Alam, M. F., Arzoumanian, Z., Baker, P. T., et al. 2021, ApJS, 252, 5
Amaro-Seoane, P., Audley, H., Babak, S., et al. 2017, arXiv:1702.00786
Artymowicz, P., & Lubow, S. H. 1996, ApJL, 467, L77
Babak, S., Petiteau, A., Sesana, A., et al. 2016, MNRAS, 455, 1665
Baker, J. G., Centrella, J., Choi, D.-I., Koppitz, M., & van Meter, J. 2006, PhRvL, 96, 111102
Balbus, S. A., & Hawley, J. F. 1991, ApJ, 376, 214
Barnes, J. E., & Hernquist, L. 1992, ARA&A, 30, 705
Barnes, J. E., & Hernquist, L. 1996, ApJ, 471, 115
Begelman, M. C., Blandford, R. D., & Rees, M. J. 1980, Natur, 287, 307
Bode, T., Bogdanović, T., Haas, R., et al. 2011, ApJ, 744, 45
Bogdanović, T., Eracleous, M., & Sigurdsson, S. 2009, ApJ, 697, 288
Bonning, E., Marronetti, P., Neilsen, D., & Matzner, R. 2003, PhRvD, 68, 044019
Bowen, D. B., Campanelli, M., Krolik, J. H., Mewes, V., & Noble, S. C. 2017, ApJ, 838, 42
Bowen, D. B., Mewes, V., Campanelli, M., et al. 2018, ApJL, 853, L17
Bowen, D. B., Mewes, V., Noble, S. C., et al. 2019, ApJ, 879, 76
Bowen, J. M., & York, J. W. 1980, PhRvD, 21, 2047
Campanelli, M., Lousto, C. O., Marronetti, P., & Zlochower, Y. 2006, PhRvL, 96, 111101
Chakrabarti, S. K. 1985, ApJ, 288, 1
Chandrasekhar, S. 1960, PNAS, 46, 253
Chapon, D., Mayer, L., & Teyssier, R. 2013, MNRAS, 429, 3114
Combi, L., Lopez Armengol, F. G., Campanelli, M., et al. 2021, arXiv:2103.15707

Cook, G. B. 2000, LRR, 3, 5
Cuadra, J., Armitage, P. J., Alexander, R. D., & Begelman, M. C. 2009, MNRAS, 393, 1423
Dain, S., Lousto, C. O., & Takahashi, R. 2002, PhRvD, 65, 104038
Damour, T., Jaranowski, P., & Schäfer, G. 2000, PhRvD, 62, 044024
d'Ascoli, S., Noble, S. C., Bowen, D. B., et al. 2018, ApJ, 865, 140
D'Orazio, D. J., Haiman, Z., & MacFadyen, A. 2013, MNRAS, 436, 2997
Derdzinski, A. M., D'Orazio, D., Duffell, P., Haiman, Z., & MacFadyen, A. 2019, MNRAS, 486, 2754
Dotti, M., Colpi, M., Haardt, F., & Mayer, L. 2007, MNRAS, 379, 956
Dotti, M., Montuori, C., Decarli, R., et al. 2009a, MNRAS Lett., 398, L73
Dotti, M., Ruszkowski, M., Paredi, L., et al. 2009b, MNRAS, 396, 1640
Dotti, M., Sesana, A., & Decarli, R. 2012, AdAst, 2012, 940568
Duez, M. D., & Zlochower, Y. 2018, RPPh, 82, 016902
Escala, A., Larson, R. B., Coppi, P. S., & Mardones, D. 2004, ApJ, 607, 765
Escala, A., Larson, R. B., Coppi, P. S., & Mardones, D. 2005, ApJ, 630, 152
Farris, B. D., Duffell, P., MacFadyen, A. I., & Haiman, Z. 2014, ApJ, 783, 134
Farris, B. D., Gold, R., Paschalidis, V., Etienne, Z. B., & Shapiro, S. L. 2012, PhRvL, 109, 221102
Farris, B. D., Liu, Y. T., & Shapiro, S. L. 2011, PhRvD, 84, 024024
Fishbone, L. G., & Moncrief, V. 1976, ApJ, 207, 962
Gallouin, L., Nakano, H., Yunes, N., & Campanelli, M. 2012, CQGra, 29, 235013
Gammie, C. F., McKinney, J. C., & Toth, G. 2003, ApJ, 589, 444
Giacomazzo, B., Baker, J. G., Miller, M. C., Reynolds, C. S., & van Meter, J. R. 2012, ApJL, 752, L15
Gold, R., Paschalidis, V., Etienne, Z. B., Shapiro, S. L., & Pfeiffer, H. P. 2014, PhRvD, 89, 064060
Gold, R., Paschalidis, V., Ruiz, M., et al. 2014, PhRvD, 90, 104030
Graham, M. J., Djorgovski, S. G., Stern, D., et al. 2015a, Natur, 518, 74
Graham, M. J., Djorgovski, S. G., Stern, D., et al. 2015b, MNRAS, 453, 1562
Hayasaki, K., Mineshige, S., & Sudou, H. 2007, PASJ, 59, 427
Healy, J., Ruchlin, I., Lousto, C. O., & Zlochower, Y. 2016, PhRvD, 94, 104020
Ireland, B., Mundim, B. C., Nakano, H., & Campanelli, M. 2016, PhRvD, 93, 104057
Kerr, R. P., & Schild, A. 2009, GReGr, 41, 2485
Khan, F. M., Mirza, M. A., & Holley-Bockelmann, K. 2019, MNRAS, 492, 256
Krolik, J. H., Volonteri, M., Dubois, Y., & Devriendt, J. 2019, ApJ, 879, 110
Lin, D. N. C., & Papaloizou, J. 1979, MNRAS, 188, 191
Liu, F. K., Wu, X.-B., & Cao, S. L. 2003, MNRAS, 340, 411
Liu, T., Gezari, S., Ayers, M., et al. 2019, ApJ, 884, 36
Lousto, C. O., Nakano, H., Zlochower, Y., Mundim, B. C., & Campanelli, M. 2012, PhRvD, 85, 124013
Lovelace, G., Boyle, M., Scheel, M. A., & Szilagyi, B. 2012, CQGra, 29, 045003
Lovelace, G., Owen, R., Pfeiffer, H. P., & Chu, T. 2008, PhRvD, 78, 084017
MacFadyen, A. I., & Milosavljević, M. 2008, ApJ, 672, 83
Marronetti, P., Huq, M., Laguna, P., et al. 2000, PhRvD, 62, 024017
Marronetti, P., & Matzner, R. A. 2000, PhRvL, 85, 5500

Mashhoon, B. 2003, arXiv:gr-qc/0311030
Matzner, R. A., Huq, M. F., & Shoemaker, D. 1998, PhRvD, 59, 024015
Mayer, L. 2013, CQGra, 30, 244008
Mayer, L., Kazantzidis, S., Madau, P., et al. 2007, Sci, 316, 1874
Merritt, D. 2004, in Coevolution of Black Holes and Galaxies, ed. L. C. Ho (Cambridge: Cambridge Univ. Press), 263
Merritt, D. 2006, RPPh, 69, 2513
Merritt, D., & Ekers, R. D. 2002, Sci, 297, 1310
Merritt, D., & Milosavljević, M. 2005, LRR, 8, 8
Mihos, J. C., & Hernquist, L. 1996, ApJ, 464, 641
Miranda, R., Munoz, D. J., & Lai, D. 2016, MNRAS, 466, 1170
Mirza, M. A., Tahir, A., Khan, F. M., et al. 2017, MNRAS, 470, 940
Moody, M. S. L., Shi, J.-M., & Stone, J. M. 2019, ApJ, 875, 66
Mundim, B. C., Nakano, H., Yunes, N., et al. 2014, PhRvD, 89, 084008
Muñoz, D. J., & Lai, D. 2016, ApJ, 827, 43
Muñoz, D. J., Lai, D., Kratter, K., & Miranda, R. 2020, ApJ, 889, 114
Muñoz, D. J., Miranda, R., & Lai, D. 2019, ApJ, 871, 84
Noble, S. C., Gammie, C. F., McKinney, J. C., & Zanna, L. D. 2006, ApJ, 641, 626
Noble, S. C., Krolik, J. H., & Hawley, J. F. 2009, ApJ, 692, 411
Noble, S. C., Krolik, J. H., Campanelli, M., et al. 2021, arXiv:2103.12100
Noble, S. C., Mundim, B. C., Nakano, H., et al. 2012, ApJ, 755, 51
Pfeiffer, H. P., Cook, G. B., & Teukolsky, S. A. 2002, PhRvD, 66, 024047
Pretorius, F. 2005, PhRvL, 95, 121101
Pringle, J. E. 1991, MNRAS, 248, 754
Rafikov, R. R. 2016, ApJ, 827, 111
Reardon, D. J., Hobbs, G., Coles, W., et al. 2016, MNRAS, 455, 1751
Rodriguez, C., Taylor, G. B., Zavala, R. T., et al. 2006, ApJ, 646, 49
Roedig, C., Krolik, J. H., & Miller, M. C. 2014, ApJ, 785, 115
Ruchlin, I., Healy, J., Lousto, C. O., & Zlochower, Y. 2017, PhRvD, 95, 024033
Saade, M. L., Stern, D., Brightman, M., et al. 2020, ApJ, 900, 148
Scheel, M. A., Giesler, M., Hemberger, D. A., et al. 2015, CQGra, 32, 105009
Schoenmakers, A. P., de Bruyn, A. G., Rottgering, H. J. A., van der Laan, H., & Kaiser, C. R. 2000, MNRAS, 315, 371
Sesana, A., & Khan, F. M. 2015, MNRAS, 454, L66
Shi, J.-M., & Krolik, J. H. 2015, ApJ, 807, 131
Shi, J.-M., Krolik, J. H., Lubow, S. H., & Hawley, J. F. 2012, ApJ, 749, 118
Springel, V., Matteo, T. D., & Hernquist, L. 2005, ApJL, 620, L79
Tagoshi, H., Ohashi, A., & Owen, B. J. 2001, PhRvD, 63, 044006
Tang, Y., MacFadyen, A., & Haiman, Z. 2017, MNRAS, 469, 4258
Tiede, C., Zrake, J., MacFadyen, A., & Haiman, Z. 2020, ApJ, 900, 43
Toth, G. 2000, JCoPh, 161, 605
Valtonen, M. J., Nilsson, K., Sillanpää, A., et al. 2006, ApJL, 643, L9
Velikhov, E. 1959, Sov. Phys. JETP, 36, 995
York, J. W. 1971, PhRvL, 26, 1656
Zilhão, M., Noble, S. C., Campanelli, M., & Zlochower, Y. 2015, PhRvD, 91, 024034
Zlochower, Y., Healy, J., Lousto, C. O., & Ruchlin, I. 2017, PhRvD, 96, 044002